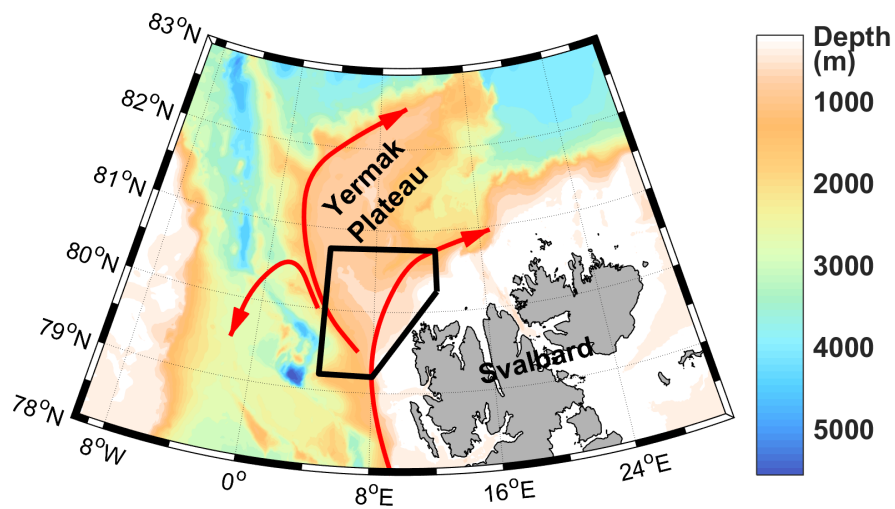# The Svalbard branch of the West Spitsbergen Current: Hydrography, transport and mixing

Master's Thesis in Physical Oceanography

by

Eivind Kolås

June 1st, 2017

UNIVERSITY OF BERGEN
GEOPHYSICAL INSTITUTE

Front figure - Overview of the study region. The black box encloses the region where data was collected. The red arrows show the different branches of the West Spitsbergen Current.

Abstract

Data from a 10 days shipboard survey in August 2015, northwest of Svalbard, are used to investigate the transport, structure and mixing of Atlantic water (AW) along the Svalbard branch and Yermak branch of the West Spitsbergen Current. Using the common definition of AW, the volume transport south and north of the Yermak Plateau (YP) is estimated to be 3.6 (3.4, 3.7) Sv and 1.1 (1.1, 1.3) Sv respectively, where the upper and lower bounds are inferred from the sensitivity to the choice of streamtubes. The current south and north of YP is horizontally symmetric, with surface-enhanced geostrophic velocities. On YP the symmetry breaks down, and the current spreads out and weakens over the flat plateau, with intensified currents near the steep continental slope. Volume transport across YP is 0.8 (0.5, 1.3) Sv. In addition to a well-defined Svalbard branch, current measurements show recirculation north of the Molly Hole. At the time of the survey, AW temperatures and salinities north of 79°N are found to be significantly higher than shown by the Monthly Isopycnal and Mixed-layer Ocean Climatology. Microstructure measurements show a net surface heating of 1-2 W m^{-2} of the AW layer. The downstream temperature and salinity gradients show cooling and freshening rates of 0.15°C and 0.016 g kg^{-1} per 100 km along path distance. The observed cooling rates cannot be accounted for by the vertical turbulent heat flux. Isopycnal diffusion in an eddy field north of YP is capable of cooling the current at observed rates, and can generate lower Arctic intermediate water in the process.

Acknowledgments

Eg vil først og fremst takke min rettleiar, Ilker Fer, som tok meg med på tokt nord for Svalbard og gav meg ei spanande oppgåve. Tusen takk for all rettleiing, og alle gjennomlesingar. Det har vore to lærerike år! Eg set stor pris på all interesse du har vist for mitt arbeid, og at eg fekk reise til Sopot på konferanse.

Eg vil òg takke min kjære, Margrete Hugaas, for all støtte gjennom studietida. Takk for alle gode innspel og forslag, og ikkje minst, takk for alle middagar og reine klede du har forsynt meg med den siste månaden. Det er ikkje godt å vite kva det hadde blitt av meg elles.

Stor takk til alle venner på og utanfor lesesalen for verdifulle diskusjonar. Spesielt takk til Hauk Løvseth og Andreas Frøyland som lyttar til alle innfall, uansett grad av fornuft.

Takk til mannskapet på Håkon Mosby, spesielt dei som jobba i byssa, og takk til alle dei som ryddar rundt meg i kvardagen. De er mine kvardagsheltar!

Til slutt, men ikkje minst, vil eg takke familien min for all ubetinga støtte dei gir. Spesielt takk til Arnt-Ove B. Kolås og Kjersti B. Kolås for gjennomlesing av oppgåva og verdifulle tilbakemeldingar.

Contents

List of Tables

List of Figures

1 | Introduction

Fram Strait, the strait between Greenland and Svalbard in figure 1.1, is the main connection between the Arctic Ocean and the Atlantic Ocean, and the only connection between the Arctic Ocean and the world's thermohaline circulation, thus making it a crucial location for ocean circulation and deep water ventilation (Aagaard et al., 1985). The cross section area of Fram Strait is roughly 600 km^2, through which enormous amounts of water flow each second. The total volume transport through Fram Strait is 9 ± 2 Sv (1 Sv $= 1 \times 10^6$ m^3 s^{-1}) northward, and 12 ± 1 Sv southward (Fahrbach et al., 2001; Schauer et al., 2004). The southward flow is restricted mainly to the western side of Fram Strait, and is associated with the East Greenland Current. On the eastern side of Fram Strait, the West Spitsbergen Current is located. The West Spitsbergen Current (WSC) is a northward flowing current and an extension of the Norwegian Atlantic current. It carries 6.6 ± 0.4 Sv of water, where 3.0 ± 0.2 Sv is Atlantic Water (AW) (Beszczynska-Möller et al., 2012). The cross section area of the Atlantic Water streamtube within WSC is 21.7 [+1.4, -1.8] km^2, which means that while the AW streamtube takes up less than 4% of the Fram Strait cross section area, more than 30% of the total inflow is AW carried by the WSC. Essentially, this means that WSC is the major heat and salt source for the Arctic Ocean (Boyd and D'Asaro, 1994; Aagaard et al., 1985), and Arctic conditions are highly influenced by the Atlantic Water inflow in the WSC. In fact, anomalies passing through Fram Strait can be traced along the Arctic Ocean boundary current (Dmitrenko et al., 2008). Figure 1.1 shows AW circulation in the Arctic Ocean, where Fram Strait and Barents Sea are the two AW inflow locations, Fram Strait being the major one. AW follows the continental slope counterclockwise around the Arctic Ocean, entering the basins along the ridges separating the basins. The counterclockwise current along the continental slope is referred to as the Arctic Ocean boundary current. About 0.8 Sv of Pacific water enters the Arctic ocean through Bering Strait (Woodgate, 2013). The main Pacific water route is along the North America continental slope, escaping the Arctic Ocean through the Canadian Archipelago and Fram Strait. Pacific water is colder and fresher compared to AW.

The AW inflow is of tremendous importance to the biology, chemistry and climate,
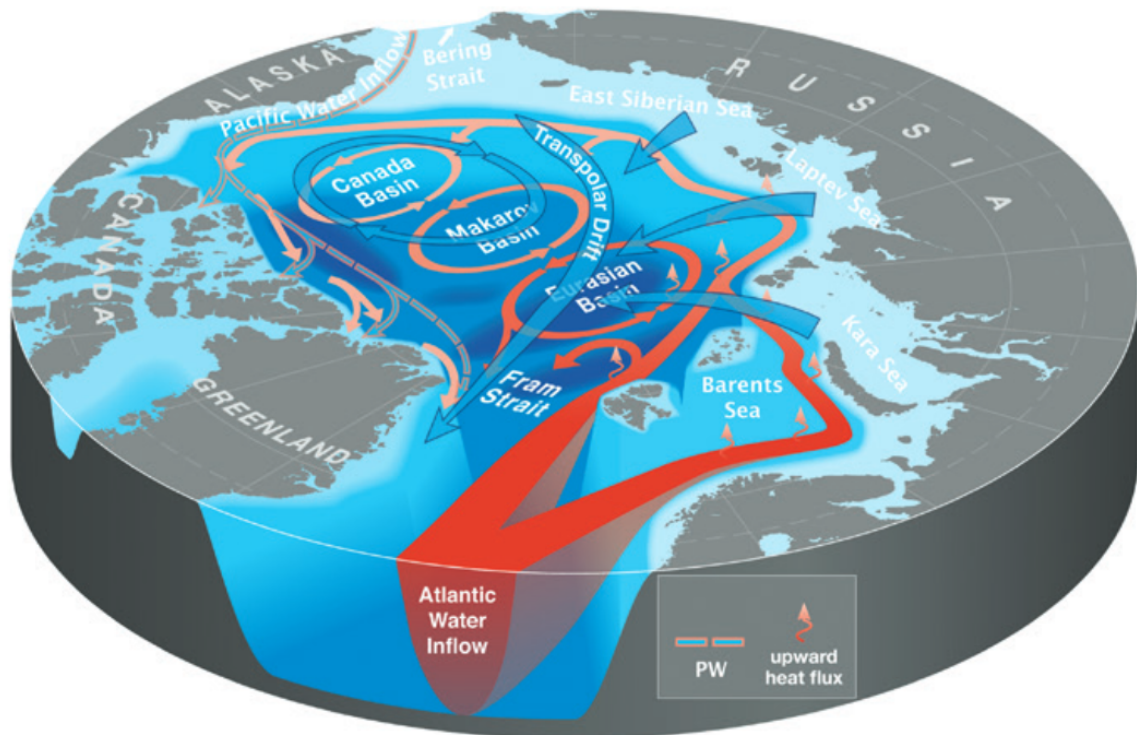
Figure 1.1 – Circulation patterns in the Arctic Ocean, where surface water is blue, Pacific Water is pink/blue and Atlantic Water is red. The upward pointing arrows indicate vertical heat loss from the Atlantic Water (Carmack et al., 2015).

both for the Arctic Ocean generally, and also for the region around Svalbard, in particular. Because of its high salinity, the fresh water content in the Arctic Ocean is directly influenced by AW. Serreze et al. (2006) estimated that 25% of the Arctic Ocean's fresh water sink is due to the AW inflow. Because of the high heat content in AW, the sea ice is very sensitive to its inflow. Both Beszczynska-Möller et al. (2012) and Onarheim et al. (2014) state that the AW inflow is getting warmer. The warmer AW is a major driver of the shrinking winter ice cover over the path of the WSC north of Svalbard (Onarheim et al., 2014). A shrinking ice cover makes the ocean more succumbing to atmospheric forcing, which is a potential positive feedback on Arctic region warming and ice melt (Rainville et al., 2011).

The Arctic biology, especially the flourishing life in and near the marginal ice zone is affected by changes in temperature, salinity and sea ice. To make accurate future predicaments about the Arctic region, it is crucial to observe changes in the AW inflow and understand the processes modifying it. The WSC is severely modified from just south of the Yermak Plateau to the north side of Svalbard; this region is the focus of this study.

This thesis is an observational study making use of the data collected from a scientific

cruise to north of Svalbard, near the Yermak Plateau, in August 2015, including hydro-
graphic profiles, horizontal current profiles and vertical profiles of ocean microstructure.
This study will first present the large scale geostrophic currents, heat budget and water
masses, and their evolution along the path of WSC. Next, the August 2015 conditions of
the WSC will be compared to the Monthly Isopycnal and Mixed-layer Ocean Climatol-
ogy (MIMOC). Finally, vertical mixing and vertical heat loss from the WSC streamtube
will be quantified. The goal of this study is to improve the general understanding of
processes modifying the Atlantic Water inflow, into the Arctic Ocean, over the YP, and
describe the importance of vertical mixing in this area.

In chapter 2 the theoretical background and the previously work done in the area
are presented. Chapter 3 describes the details about the instrumentation used and
the data collected, together with the methods for various calculations. The results are
presented in chapter 4, followed by a discussion in chapter 5. Conclusions are given in
chapter 6.

2 | Background

2.1 Circulation Pattern of the West Spitsbergen Current

The WSC flows at a steady pace of about 0.25 m s^{-1}, following the 1000-m isobath, from Bear Island at 74°30′N to the southern flanks of the Yermak Plateau (YP) at 79°30′N (Boyd and D'Asaro, 1994). YP is a shallow plateau with depths around 500 m, stretching north-northwestward from Svalbard. An important geographical feature on the YP is the divergence of isobaths. Figure 2.1 shows a sketch of the WSC paths along Spitsbergen and YP. The mean net volume transport in the WSC, measured along 78°50′N in the period 1997-2010, is 6.6 ± 0.4 Sv, where 3.0 ± 0.2 Sv is Atlantic Water (Beszczynska-Möller et al., 2012). Atlantic Water entering the Arctic is defined as water with temperature, $\theta \geq 2$°C, and practical salinity, $S > 34.88$. Observations show that the WSC splits into two branches where the isobaths diverge near the YP at 79°30′N, an outer branch following the 1000-m isobath, and an inner branch following the 400-m isobath (Aagaard et al., 1987; Farrelly et al., 1985). The WSC has a strong barotropic component, hence, if the mixing and temporal variability are small, it should be possible to track the two branches along the preferred isobaths, based on their initial upstream potential vorticity (Perkin and Lewis, 1984). In other words, if the potential vorticity is conserved, the current will follow the f/H contours as it flows northward, where f is the Coriolis parameter and H is the depth of the water column. The inner branch flowing over the Yermak Plateau along the 400-m isobath has a 40 km wide core and seems to follow the isobath closely along Svalbard, with little mixing or offshore excursion (Aagaard et al., 1987). The outer branch however, has a 60 km wide core and does not seem to follow the 1000-m isobath as closely (Aagaard et al., 1987). Observations suggest that a part of the outer branch detaches from the 1000-m isobath and recirculates on the eastern side in Fram Strait, contributing to warm and salty water in the southward flow, adjacent to the Greenland margin (Aagaard et al., 1987; Farrelly et al., 1985; Beszczynska-Möller et al., 2012; Hattermann et al., 2016). The main recirculation route is found to be on the northern rim of the Molly

Figure 2.1 – The branches of the West Spitsbergen Current (WSC). At 79°30′N the WSC splits into an inner branch following the 400-m isobath and an outer branch following the 1000-m isobath. A part of the outer branch detaches and recirculates on the eastern side of Fram Strait, north of the Molly Hole (MH)
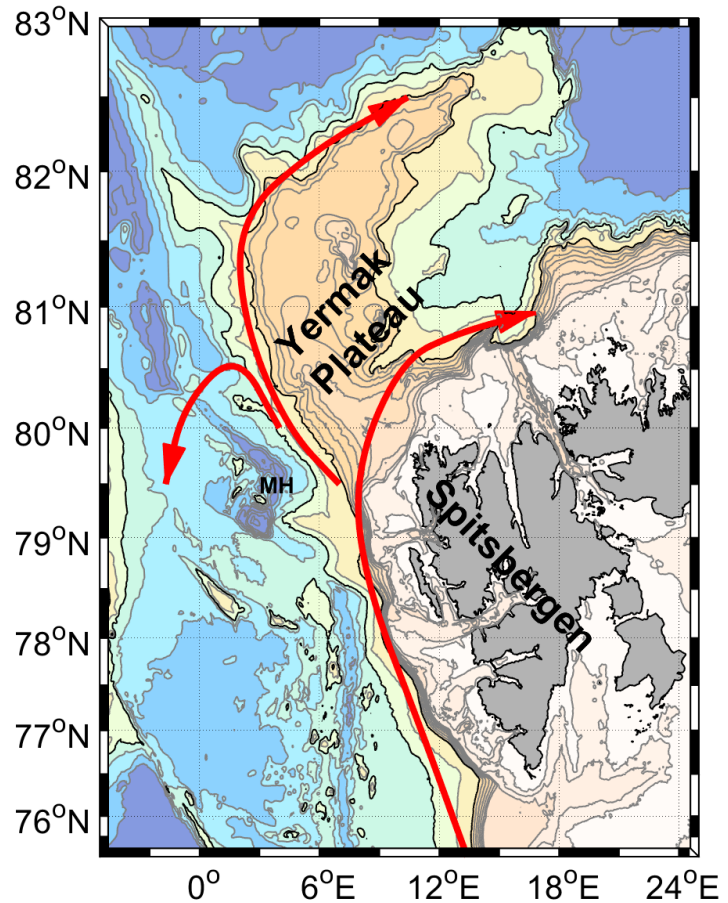
Hole at about 80°N and 4°E (Hattermann et al., 2016). The recirculating branch is marked by the cyclonic pointing red arrow north of the Molly Hole (MH) in figure 2.1. The MH is deeper than 3000 m, and some places as deep as 6000 m. The part of the outer branch not recirculating in Fram Strait is thought to follow the 1000-m isobath around YP, rejoining the inner branch where the isobaths converge north of Svalbard at approximately 80°30′N and 13°E (Perkin and Lewis, 1984). Aagaard et al. (1987) did not observe any Atlantic Water from the outer branch rejoining the inner branch north of Svalbard during the cruise with *Polarsirkel* in 1977, and state that the outer branch either detaches from the plateau north of 80°N, or it is so thoroughly mixed downstream that it is unrecognizable. However, more resent observations made by Cokelet et al. (2008), Våge et al. (2016) and Meyer et al. (2016) suggest the presence of an outer branch north of Svalbard, confirming that the outer branch traces the edge of the YP.

Perkin and Lewis (1984) observed intrusive layering of Atlantic Water on the northern slope of the Yermak Plateau at about 82°30′N and 10°E, from CTD profiles taken during March and April 1981. However, geostrophic velocity calculations, based on dynamic height, did not show currents significantly different from zero (Perkin and Lewis, 1984). Both Padman and Dillon (1991) and Perkin and Lewis (1984) explain that the outer branch contains a series of eddies of diameter about 20 km, that are

shed where the two branches split. These eddies play a major role in how much AW recirculates in Fram Strait, and therefore, a major role in the salt and heat budget of the Arctic Ocean (von Appen et al., 2016; Hattermann et al., 2016). Furthermore, the eddies generated in Fram Strait show large seasonal variability, with eddy kinetic energy three times higher during winter than late summer, suggesting that the offshore branch of the WSC is weaker during summer than winter (von Appen et al., 2016). The implications of the eddies generated along the WSC is ongoing research (von Appen et al., 2016; Hattermann et al., 2016). Due to sea ice, observing the outer branch along the Yermak Plateau north of about 80°30′N is difficult. The inner branch continues as a topographically trapped boundary current downstream, contributing to the circumpolar boundary current. Between Fram Strait and the Lomonosov Ridge (the ridge between the Eurasian basin and the Makarov Basin, figure 1.1), the boundary current slows down from about 0.25 m s^{-1} to 0.06 m s^{-1}, and changes structure from a mainly barotropic flow to a baroclinic flow (Pnyushkov et al., 2015).

2.2   Water mass Transformation along the West Spitsbergen Current

As the Atlantic Water flows towards the Arctic Ocean, its properties are influenced by atmospheric conditions, surrounding waters, and sea ice floes. As the temperature and salinity are changed, new water masses are formed. Table 2.1 gives an overview of the different water masses found in the Iceland and Greenland seas, as first defined by Swift and Aagaard (1981), and later modified by Aagaard et al. (1985). The column showing Absolute Salinity, S_A, was calculated from the practical salinity units, using the Gibbs SeaWater (GSW) Oceanographic Toolbox (McDougall and Barker, 2011). S_A was calculated for 80°N and 10°E, and rounded to the nearest hundredth.

Using observations extending from Bear Island to the Yermak Plateau, Boyd and D'Asaro (1994) found that the warm core of the WSC cooled at a rate of 0.5°C/100 km between January and February 1989. From just south of the Yermak Plateau to the north of Svalbard, Cokelet et al. (2008) observed a cooling of 0.19°C/100 km during October and November 2001, comparable to Saloranta and Haugan (2004) who calculated a long term (50 years) summer-mean cooling (August-October) of 0.20°C/100 km. In comparison, the long term winter-mean cooling (March-May) was 0.31°C/100 km (Saloranta and Haugan, 2004). The calculations done by Saloranta and Haugan (2004) were based on data collected in the period from 1949 to 1999, over the WSC core, between 74° and 79° N. In 1910, Helland-Hansen and Nansen (1912) calculated a 0.20°C/100km cooling between 75°N and 79°N, along the WSC. It is worth noting

Table 2.1 – Water masses in the Iceland and Greenland seas as defined by Swift and Aagaard (1981) and Aagaard et al. (1985). Absolute Salinity (S_A) has been calculated from the practical salinity using the Gibbs SeaWater Oceanographic Toolbox (McDougall and Barker, 2011). S_A was calculated for 80°N and 10°E, and rounded to the nearest hundredth.

Abbr.	Name	Salinity (S) [psu]	Absolute Salinity (S_A) [$g\ kg^{-1}$]	Temperature (θ)
AW	Atlantic Water	$S > 34.88$	$S_A > 35.05$	$\theta \geq 2°C$
LAIW	Lower Arctic Intermediate Water	$S > 34.88$	$S_A > 35.05$	$2°C > \theta \geq 0°C$
UAIW	Upper Arctic Intermediate Water	$34.88 \geq S \geq 34.7$	$35.05 \geq S_A \geq 34.87$	$\theta < 1°C$
DW	Deep Water	$34.96 \geq S > 34.88$	$35.13 \geq S_A > 35.05$	$\theta < 0°C$
PW	Polar Water	$S < 34.4$	$S_A < 34.56$	$\theta < 0°C$
PIW	Polar Intermediate Water	$34.7 > S \geq 34.4$	$34.87 > S_A \geq 34.56$	$\theta < 0°C$
ASW	Arctic Surface Water	$34.7 > S \geq 34.4$ $34.88 \geq S \geq 34.7$	$34.87 > S_A \geq 34.56$ $35.05 \geq S_A \geq 34.87$	$\theta > 0°C$ $\theta > 2°C$

that when Helland-Hansen and Nansen (1912) measured the northward cooling, it took 23 days between deployments in their southern most section and their northern most section, hence, they corrected their section-mean temperature by the probable change in the difference of time. That is, they found a section-mean temperature at a common date by correcting for an increase in temperature of 0.10°C/10 days.

The salinity has as south-north gradient along the WSC from Bear Island to north of Svalbard. The core of the WSC freshens as it flows northward as a result of melting of sea ice and mixing with fresh and cold shelf waters. For a layer between 100 m and 500 m, Cokelet et al. (2008) found a northward freshening of 0.013/100 km, and Saloranta and Haugan (2004) obtained a mean summer freshening of 0.010/100 km, measured in practical salinity scale.

The cooling gradient along the WSC is thus mapped fairly well, however, the relative
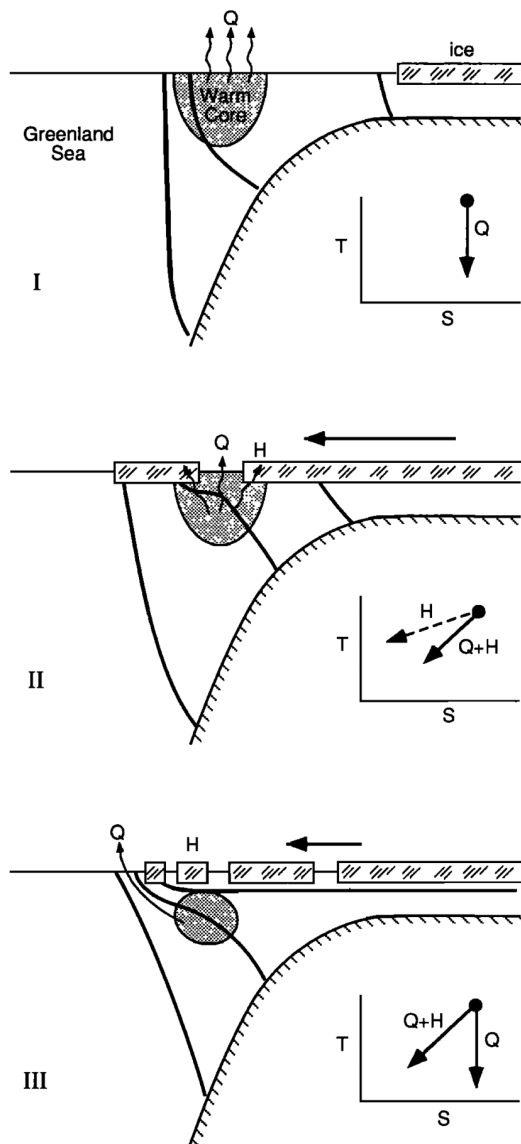
Figure 2.2 – Conceptual stages of the cooling of Atlantic Water in the West Spitsbergen Current (Boyd and D'Asaro, 1994). Q is Atlantic water heat loss to the atmosphere, while H is Atlantic water heat loss to the sea ice. In *I* all the heat is lost to the atmosphere, and the TS-diagram shows the adjoining Gade line. In *II*, sea ice has moved over the Atlantic Water core, and heat is lost to the ice and the atmosphere. The TS-diagram shows the Gade line for when all the heat is lost to the ice, and when the heat is lost to a combination of ice and atmosphere. In *III*, the Atlanic Water core is separated from the surface, but heat is still lost along the isopycnals to the atmosphere west of the sea ice. The black lines are isopycnals.

role of the different cooling processes is not clear. The cooling of the WSC can be roughly described as a three-stage process (Boyd and D'Asaro, 1994). The three stages described below are sketched in figure 2.2, where Q is the heat loss from the Atlantic Water to the atmosphere, and H is the heat loss from Atlantic Water to ice. Figure 2.3 shows the different water masses in a TS-diagram, where the red lines are the Gade lines at a specific Q/H ratio. A Gade line is the path the water mass transformation follows. $Q/H = 0$ means all the heat is lost to sea ice, while $Q/H = \infty$ means all the heat is lost to the atmosphere. The three stages can be summarized as follows.

I) As the WSC carries Atlantic Water from Bear Island to Svalbard, the warm core is close to the surface, only separated by a deep and warm mixed layer. During this transport, the Atlantic Water is under direct influence of atmospheric cooling. When the Atlantic Water core is at the surface, with little or no sea ice cap, as indicated by the upper sketch in figure 2.2, H approaches zero, and the transformation path is indicated

by the red Gade line marked $Q/H = \infty$ in figure 2.3. Cooling of the Atlantic Water without changing the salinity of the water mass will result in the formation of a denser water mass, called Lower Arctic Intermediate Water (LAIW), defined as water with the same salinity as AW, but temperatures between $0°$ and $2°$C (Swift and Aagaard, 1981). LAIW is crucial in the thermohaline circulation of the Atlantic Ocean, because it is the densest water flowing over the Greenland-Scotland ridge (Aagaard et al., 1985). Water denser than LAIW is confined in the Arctic Mediterranean.

II) When AW in WSC approaches the waters north of Spitsbergen, it encounters sea ice as shown by the middle sketch in figure 2.2. If heat is lost only to melting the ice, the transformation path would follow the red line marked $Q/H = 0$ in figure 2.3. The ice not only cools the Atlantic Water, but also freshens it, creating a less dense water mass called Arctic Surface Water (ASW). See table 2.1 for properties of ASW. ASW formation is an important first step in forming the cold halocline layer (CHL) that separates the Atlantic Water from the surface layer downstream (Thomas and Dieckmann S., 2009, ch. 3, p. 86). As the WSC carries Atlantic Water from Svalbard towards Franz Josef Land, the sea ice concentration increases, the ASW layer thickens, and cold, brine-rich waters from the Barents Sea advect over AW to create the cold halocline layer, which can be found throughout the Arctic Ocean (Aagaard et al., 1981). CHL is the layer between AW and the surface that is close to the freezing point, but well stratified in salinity, preventing AW from mixing upwards, and thereby, preventing oceanic heat from melting sea ice or being lost to the atmosphere. The CHL is commonly found in the Amundsen Basin (the northern part of the Eurasian Basin), the Makarov Basin, and the Canada Basin (see figure 1.1).

III) When AW is separated from surface, and so, is not directly cooled by the atmosphere or melting of sea ice, the warm core may still continue to cool (lower sketch in figure 2.2). Boyd and D'Asaro (1994) state that this cooling is most likely due to eddy driven mixing along isopycnals. During the winter cruise in 1989, Boyd and D'Asaro (1994) observed isopycnals passing through the subducted warm core of WSC, and outcropping 5-10 km to the west of the core. Also Cokelet et al. (2008) observed outcropping isopycnals passing through the sub-surface warm core just south of the Yermak Plateau, but these isopycnals outcropped 140 km seaward. If the outcropping occurs in an ice free region, it is likely that LAIW is formed. If sea ice has advected over the outcropping icopycnals, it is likely that fresher, colder water will form. The red Gade line marked $Q/H = 1$ in figure 2.3 shows the transformation path when an equal amount of heat is lost to atmosphere and ice, while the red Gade line marked $Q/H = 5$ shows the transformation path when the heat loss to the atmosphere is five times greater than the heat loss to ice. Horizontal intrusions may also spread the upward-diffused heat seaward and maintain the cold halocline above the warm core
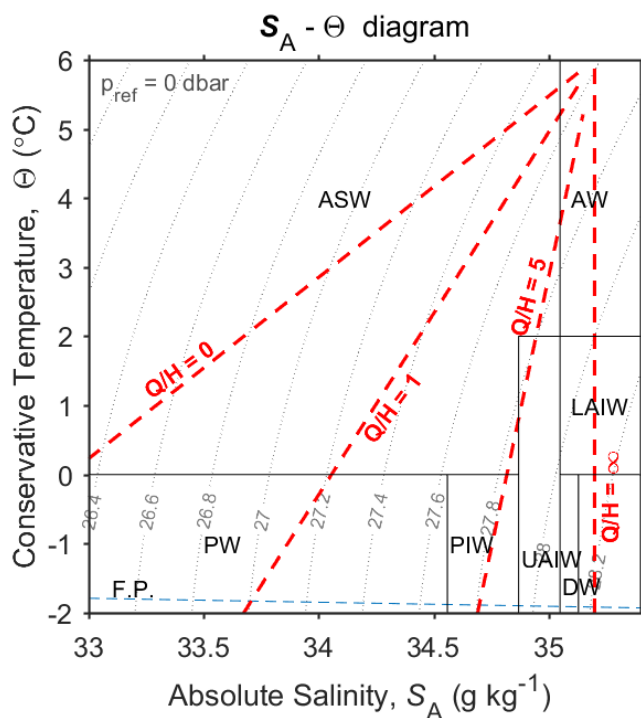
Figure 2.3 – Water mass transformation sketch. The black boxes show the different water masses as defined by Swift and Aagaard (1981) and Aagaard et al. (1985): Arctic Surface Water (ASW), Atlantic Water (AW), Lower Arctic Intermediate Water (LAIW), Upper Arctic Intermediate Water (UAIW), Deep Water (DW), Polar Water (PW), and Polar Intermediate Water (PIW). The red Gade lines show the transformation paths AW will follow depending on the heat loss. Q is AW heat loss to the atmosphere, while H is AW heat loss to the sea ice. $Q/H = 0$ shows the Gade line when all the heat is lost to sea ice, $Q/H = 1$ is the Gade line when AW heat is lost equally to ice and atmosphere, $Q/H = 5$ is the Gade line for five times more heat lost to the atmosphere, and $Q/H = \infty$ is the Gade line when all the heat is lost to the atmosphere.

(Cokelet et al., 2008). These intrusions can occur due to freezing and brine exclusions on the continental shelf, or from interleaving across fronts of different water masses.

The cooling ot the WSC core measured by Cokelet et al. (2008) is equivalent to a heat loss of 310 W m^{-2} from the layer between 100 m and 500 m. Saloranta and Haugan (2004) obtained a mean summer heat flux of 330 W m^{-2} for the same layer, using the same mean horizontal velocity in the calculations (0.1 m s^{-1}). For comparison, the mean winter heat flux for the same layer is estimated to be 1050 W m^{-2} (Saloranta and Haugan, 2004). Aagaard et al. (1987) calculated a vertical heat flux of 230 W m^{-2} for the 100 m to 200 m layer, using a mean velocity of 0.2 m s^{-1}. Cokelet et al. (2008) got a heat flux of 240 W m^{-2} using the same current speed and layer thickness as Aagaard et al. (1987). An upper bound for the vertical heat flux to the ocean surface during summer, neglecting all horizontal processes, is estimated to be about 520 W m^{-2} in the 0 to 500 m layer (Cokelet et al., 2008), and the long term mean for the 0 to 500 m layer was estimated to be 460 W m^{-2} (Saloranta and Haugan, 2004).

The heat flux needed to obtain the observed rates of cooling of the WSC is, as stated above, very large. Padman and Dillon (1991) explain that the steep slopes and prominent topography of the Yermak Plateau play an important role in modifying the Atlantic Water inflow into the Arctic Ocean. Using data from a microstructure profiler, Sirevaag and Fer (2009) found large turbulent fluxes and rate of Atlanic Water heat loss along the path of the WSC. Mixed layer heat fluxes within or close to the WSC were between 200-300 W m^{-2}, hence measured heat fluxes along the WSC support the inferred heat fluxes, based on observed cooling, as reported by Aagaard et al. (1987); Saloranta and Haugan (2004); Cokelet et al. (2008).

Once the Atlantic Water is submerged and covered by the CHL, the vertical mixing, and the heat flux to the atmosphere become very small. Padman and Dillon (1991) analyzed data collected from an ice camp drift that was located on the northeastern slopes of the Yermak Plateau during March and April 1989 (82°30′N, 8°E). They found that the upward heat flux from the Atlantic layer over the Yermak Plateau slope was 25 W m^{-2}, and of that about 6 W m^{-2} entered the mixed layer. Padman and Dillon (1991) also observed that isopycnal displacements over the slope had a diurnal signal, potentially caused by tidal currents. Perkin and Lewis (1984) found, from CTD stations along the northeastern slopes of the Yermak Plateau (82°30′N, 10°E), that the AW temperature maximum had a "triple peak" structure, with step like profile above and below the warm Atlantic water, suggesting that the vertical mixing is at times weak enough to make double-diffusive processes important. A double-diffusive process is induced by different molecular rates of diffusion for heat and salt. Outside the WSC, near the northeastern flank of the Yermak Plateau, Sirevaag and Fer (2009) found an average vertical heat flux of 2 W m^{-2}, comparable to the annual oceanic heat flux of 3-4 W m^{-2} to the Arctic pack ice as reported by Krishfield and Perovich (2005). Away from the Yermak Plateau and the continental shelf, the vertical diffusivity seems to become too small to account for any significant heat loss from the Atlantic Water. In fact, both Lenn et al. (2009) and Fer (2009) find that the vertical diffusivity in the central Arctic and along the boundary current in the Arctic, is orders of magnitude too small to account for the oceanic heat flux causing the Atlantic Water to cool as much as observed beneath a cold halocline under sea ice. Lateral mixing, shelf-basin exchange, and intrusions of cold shelf water is probably the main cooling mechanisms along the Arctic shelves (Sirevaag and Fer, 2009; Carmack et al., 2015).

During a scientific cruise to the shelfbreak and continental slope north of Svalbard at about 30°E, during September 2012, Våge et al. (2016) observed two possible mechanisms for lateral exchange. One was an anticyclonic eddy, with a AW core, located 50 km offshore from the AW boundary current. Evidence supported that this eddy had recently detached from the boundary current (Våge et al., 2016). Eddies detaching

from the boundary current can occur as a result of baroclinic instabilities (von Appen et al., 2016). The other mechanism was wind-driven upwelling that took place during the time of the survey. Upwelling and downwelling can diverge AW from the boundary current, and is a familiar phenomenon in the Canadian Basin (von Appen and Pickart, 2012).

2.3   Interannual variability in the West Spitsbergen Current

Since 1967, a fairly continuous record of hydrographic conditions in the WSC has been collected. Dickson et al. (2000) compared a time series of hydrographic data along a section westward from Sørkapp (South cape) on Svalbard with changes in the North Atlantic Oscillation (NAO) between 1967 and 1999. NAO is a large-scale motion of atmospheric mass between Iceland and the Azores. During winter, NAO accounts for more than one-third of the total variance in sea level pressure, and it is the most dominant mode of atmospheric behavior over the North Atlantic throughout the year (Dickson et al., 2000). NAO alternates between an intense Iceland low with rapidly increasing pressure towards the Azores and a pattern where the anomalies are reversed. During winter NAO anomalies with intense Iceland low, Dickson et al. (2000) found that the Atlantic inflow streams (Fram Strait and Barents Sea) were 1°C to 2°C warmer than normal. Dickson et al. (2000) state that the NAO pattern currently explains 60% of the temperature variance in the Sørkapp hydrographic section time series.

Saloranta and Haugan (2001) produced an ensemble (E1) of measurements taken just south of the splitting of the WSC (79°30′N), along the upper continental slope. The E1 ensemble gives a time series from 1969 to 1997. This time series shows temperature and salinity maxima in 1970, 1984, and 1992 (Saloranta and Haugan, 2001). Saloranta and Haugan (2001) find that the correlation between the E1 time series and the NAO index is lower than the correlation between the Sørkapp data and the NAO index. Only when correlating the time series with no time lag did Saloranta and Haugan (2001) get a correlation coefficient significantly different from zero at 95% level (r=0.67). However, both Dickson et al. (2000) and Saloranta and Haugan (2001) note that the time series correlate better in the 80s and 90s than in the 70s. This time dependent correlation could be caused by the center of the NAO having shifted eastward in the 80s and 90s compared to the 50s and 60s (Hilmer and Jung, 2000).

In addition to the interannual variations in the hydrography of the WSC, there is evidence supporting a trend where the Atlantic Water entering the Arctic Ocean is becoming warmer. Onarheim et al. (2014) observed a 0.3°C per decade warming of the

Atlanic Water, that is, the Atlantic Water temperature has increased 1.1°C since 1979, a trend significant at the 95% level. These observations are based on autumn data from the Sørkapp section, between 1979 and 2012. Beszczynska-Möller et al. (2012) observed a positive linear trend in the mean Atlantic Water temperature of 0.06°C per year between 1997 and 2010. These measurements were based on a array of moorings in Fram Strait along 78°50′N. The winter ice concentration north of Svalbard shows a $10\% \pm 3\%$ decrease in the period 1979 to 2012, based on satellite images (Onarheim et al., 2014). Onarheim et al. (2014) state that the warmer Atlantic Water is a major driver of the shrinking winter ice cover over the path of the WSC north of Svalbard.

Schauer and Beszczynska-Möller (2009) analyzed data from the mooring section in Fram Strait (78°50′N), between 1997 and 2008, and calculated the annual mean oceanic heat transport into the Arctic by the WSC. They found that the heat transport increased from 26 TW in 1998 to 50 TW in 2004 (1 TW = 1×10^{12} watts). From 2004 to 2006, the heat transport decreased to 36 TW, even though the temperature of the WSC waters continued to increase. Schauer and Beszczynska-Möller (2009) explained that the temperature of the returning waters in the EGC also increased, hence, the heat brought into the Arctic by the WSC did not stay in the Arctic Ocean, but exit with the East Greenland Current. To calculate an accurate heat transport into the Arctic Ocean, a closed integral over all heat sources and heat sinks is needed.

Even though measurements of the hydrography in the WSC were made even earlier than what was presented by Helland-Hansen and Nansen (1912), reliable time series only exist from the late 60s. This time period is not long enough to conclude whether observed trends are low frequency oscillating variations or linear trends. Nonetheless, the Arctic Ocean is undergoing major physical changes, and it is probable that the loss of sea ice will enhance the atmospheric forcing on the ocean, increase vertical mixing in the upper layer, and potentially increase the amount of heat extracted from the warm Atlantic Water below a cold halocline (Carmack et al., 2015; Fer, 2014; Rainville et al., 2011).

3 | Data and Methods

3.1 Data

The data set analyzed in this thesis was collected onboard the Research Vessel Håkon Mosby during a scientific cruise to Fram Strait from August 12th to 21st, 2015. The cruise was a part of the research project *"On Thin Ice (NICE): Role of Ocean Heat Flux in Sea Ice Melt"*, where the overall objective is to study the role of diapycnal mixing for the heat budget of the Arctic Ocean, the role of ocean heat flux in modulating the ice thickness and area, and the associated feedbacks. Three moorings were deployed near the ice edge in summer 2014, and the primary aim of the cruise in August 2015 was to collect these moorings. In addition, process studies of ocean mixing in response to wind and tide forcing were planned west and north of Spitsbergen.

The instruments used to collect data onboard Håkon Mosby were CTD/LADCP (conductivity, temperature, depth / lowered acoustic Doppler current profiler), VMP (vertical micro-structure profiler) and VMADCP (vessel mounted acoustic Doppler current profiler). Figure 3.1 shows the station map for the subset of data used in this study. The blue diamonds indicate where the moorings were located (not used in this study), the blue dots show the CTD/LADCP stations, while the red circles show the VMP casts. R1 to R4 indicate the location for repeated station where only the VMP was deployed repeatedly. In total, 61 CTD/LADCP casts, and 105 VMP casts were done, however, this thesis will only be analyzing 46 CTD/LADCP casts and 85 VMP casts, as the rest of the casts were done in the Nordfjord, an extension to the Isfjord on Svalbard.

Section A took approximately 20 hours to complete with all the CTD/LADCP stations and VMP casts. Section B took 11 hours to complete, while section C was completed in 20 hours. The repeat stations, R1-R3, lasted for 12 hours, while repeat station R4 lasted for 18 hours. Table 3.1 shows an overview of the starting time and ending time of the different sections and repeated stations.

In addition to the data collected on the cruise, this thesis will be using data from the Monthly Isopycnal & Mixed-layer Ocean Climatology (MIMOC), and the Arctic Ocean Tidal Inverse Model (AOTIM-5). All the data sets are described below. For

Figure 3.1 – Station map for cruise August 2015. CTD/LADCP stations and VMP casts are shown with markers as indicated in the legend. During the repeat stations R1 to R4, only VMP is deployed. Moorings are labelled Y1 to Y3. Sections A, B and C are indicated by their edge stations with corresponding numbers. Isobaths are at 100-m interval down to 1000 m, and 500-m interval thereafter. The 1000 m and 2000 m isobaths are marked with black. (Fer, 2015).
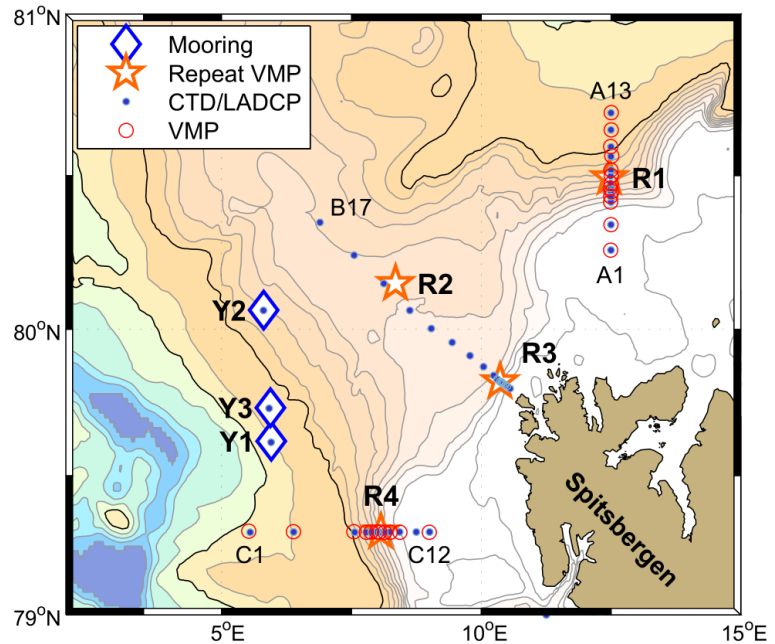
more information about the instrumentation and processing, the reader is referred to the cruise report (Fer, 2015).

3.1.1   Conductivity Temperature Depth profiler (CTD)

The CTD rosette consisted of a SBE 911plus CTD, a 24 position SBE 32 Carousel (fitted with only one 10 liter Niskin sampling bottle), a Benthos altimeter (200 kHz), and the two acoustic Doppler current profilers. The complete CTD rosette is shown in figure 3.2a.

The SBE 911plus CTD sampled data on both down and upcast. The accuracy of the temperature and conductivity sensor is given to be ±0.001 °C and ±0.0003 S/m respectively, and the accuracy of the pressure sensor is $\pm0.015\%$ of full scale range. The Benthos altimeter measured distance from the CTD rosette to the bottom, and allowed for profiling close to the bottom. For each cast, at the deepest sampling level, a water sample was collected for salinity calibration.

The SBE 911plus CTD, provides in situ temperature, T and practical salinity, S (among other variables). For this thesis, in situ temperature will be converted to Conservative Temperature, Θ, and practical salinity will be converted to Absolute Salinity, S_A. For more information about this conversion, see section 3.2.1.

Table 3.1 – Overview of the duration of the different sections and repeated stations. All times are in Coordinated Universal Time (UTC). Figure 3.1 shows the location of the different stations. For more information about the different stations, the reader is referred to the cruise report (Fer, 2015).

Section	Start		End		Duration
	Station	Date / time	Station	Date / time	
Section A	A13	August 14th / 0717 UTC	A1	August 15th / 0311 UTC	19.9 hours
	R1	August 15th / 0612 UTC		August 15th / 1817 UTC	12.1 hours
Section B	B1	August 15th / 2359 UTC	B17	August 16th / 1112 UTC	11.2 hours
	R2	August 16th / 1353 UTC		August 17th / 0215 UTC	12.4 hours
	R3	August 17th / 0615 UTC		August 17th / 1812 UTC	12.0 hours
Section C	C1	August 18th / 0109 UTC	C12	August 18th / 2123 UTC	20.2 hours
	R4	August 18th / 2311 UTC		August 19th / 1701 UTC	17.8 hours

3.1.2   Current Profiling

Horizontal currents were measured using an acoustic Doppler current profiler (ADCP). An ADCP is a device that has three or four transducers angled in different directions. The transducers send out sound pulses at a specified frequency, in known directions through the water. The sound pulses reflect from suspended particles in the water column, and depending on the velocity of these particles, the frequency of the returned sound pulses shift. This is known as the Doppler effect. Hence, one can calculate the velocity of the particles in the water by knowing the initial frequency, the reflected frequency (after a Doppler shift), the speed of sound in water, and the relative speed of the ADCP device. Equation 3.1 shows how the variables relate to one another (Cutnell and Johnson, 2013, ch. 16.9, p. 489).

$$\omega = \frac{c + v_r}{c + v_i} \cdot \omega_0 \tag{3.1}$$
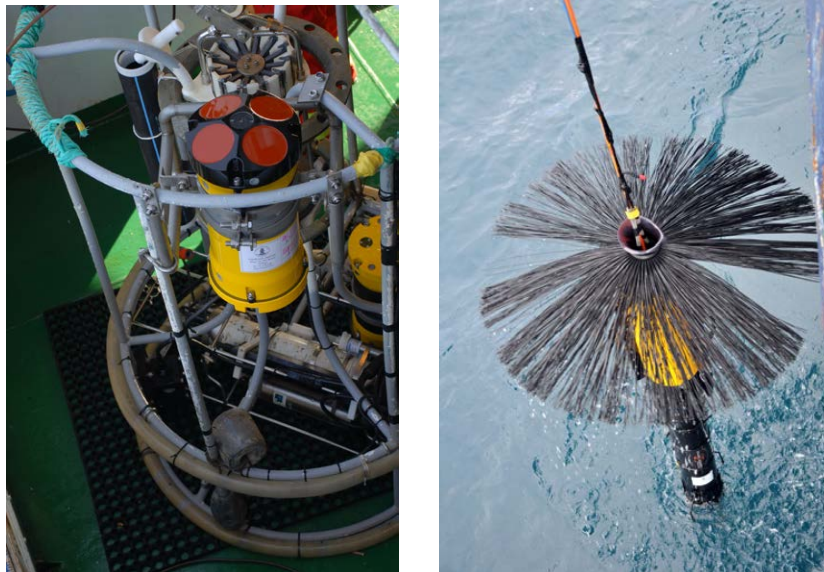
(a) CTD rosette equipped with SBE 911plus CTD, a 24 position SBE 32 Carousel (fitted with only one 10 liter Niskin sampling bottle), a Benthos altimeter (200 kHz), and the two LADCPs (6000 m-rated 300 kHz Sentinel Workhorses)(Fer, 2015)

(b) Vertical microstructure profiler (VMP) being deployed from RV Håkon Mosby. The brushes in the back provide drag, and set the sink velocity together with the buoyancy elements (yellow) (Fer, 2015)

Figure 3.2 – CTD rosette and VMP

ω is the reflected frequency, c is the speed of sound in water, v_r is the relative velocity of the ADCP device, v_i is the velocity of the particle in the water, and ω_0 is the specified initial frequency.

Lowered-ADCP (LADCP)

The lowered Acoustic Doppler Current Profiler (LADCP) system is composed of two ADCPs mounted on the CTD rosette in order to obtain current profiles. The ADCPs were 6000 m-rated 300 kHz Sentinel Workhorses with internal batteries, installed on the CTD rosette with one pointing upwards and one pointing downwards, configured to sample in master/slave mode to ensure synchronization. The ADCP looking up can be seen in figure 3.2a, it is the yellow device with four red "eyes" looking upwards in different directions. The four "eyes" hold the transducers. The vertical bin size was set to 8 m for each ADCP, with no blanc distance. Data from the first bin in each cast was discarded during post processing, due to large side lobe effect. Horizontal currents profiles are obtained using the Lamont-Doherty Earth Observatory (LDEO) Software

v.IX.12 (by A.M. Thurnherr), which is an implementation of the velocity inversion method described in Visbeck (2002), constrained by velocities from ship navigation, bottom tracking as well as shipboard ADCP. For processing with multiple constraints, such as applied here, Thurnherr (2010) estimate overall root mean square LADCP velocity errors less than 3 cm/s.

Vessel-mounted ADCP (VMADCP)

The vessel mounted Acoustic Doppler Current Profiler (VMADCP) mounted on RV Håkon Mosby was a 75 kHz RDI ADCP. It collected velocity profiles continuously below the ship throughout the cruise. The blank distance was 8 m (no data returned for the first 8 m), the bin size was 8 m (data returned as 8 m vertical average), and the number of bins was 100. During the cruise, the ADCP was set to return short term average (STA) every 60 s, and long term average (LTA) every 300 s. Final profiles, with 5 minutes average in time, are obtained using the CODAS (Common Ocean Data Access System) processing software maintained at University of Hawaii (Firing et al., 1995).

3.1.3   Vertical Microstructure Profiler (VMP)

Ocean microstructure measurements were made using a vertical microstructure profiler, VMP2000. The VMP used can be seen in figure 3.2b. It is manufactured by Rockland Scientific International, Canada. A VMP measures dissipation-scale turbulence, and in order to do so accurately, it is crucial that the VMP free-falls at a known, steady pace. The VMP's speed through water is estimated from three parameters: the drag coefficient, the VMP volume, and hull compressibility (Fer et al., 2014). The more accurate the sink velocity is estimated, the more accurate the dissipation rate measurements will be. The VMP used on the cruise had brushes at the rear end to create drag, and buoyancy element to give it the nominal sink velocity of 0.6 m/s. In figure 3.2b the brushes and the yellow buoyancy elements can be seen. The VMP was equipped with high-accuracy SBE CT sensors, a pressure sensor, microstructure velocity shear probes, one high-resolution temperature sensor, one high-resolution microconductivity sensor, and three accelerometers. During casts, real time signals and signal-derivatives are transmitted to the ship through a 2500-m long tether.

The turbulent dissipation, ε, is the rate of loss of turbulent kinetic energy (TKE) per unit mass. TKE is lost to heat due to fluid viscosity. Turbulent dissipation, when assuming turbulence is isotropic, can be expressed as

$$\varepsilon = \frac{15}{2}\nu\overline{\left(\frac{\partial u}{\partial z}\right)^2} \tag{3.2}$$

where ν is the kinematic viscosity with units $[\mathrm{m}^2/\mathrm{s}]$, overbar denotes averaging, and the derivative $\partial u/\partial z$ is the vertical velocity shear of the velocity component u (Thorpe, 2007, ch. 2.3). Isotropic turbulence means that the turbulent motion and its derivatives are the same in all directions, allowing for the very simplified equation 3.2.

The time series of the velocity component u or v can be used to compute the spatial derivative (shear) such that $\partial u/\partial z = (1/U)\partial u/\partial t$, where U is the nominal sink velocity (Thorpe, 2007, ch. 2.5). However, for small-scale velocity gradients the shear spectra was used to obtain ε. Following the Taylor hypothesis, that is, assuming that the turbulent structure is "frozen" and passive as the VMP sinks through it, the following equations relate to one another (Thorpe, 2007, ch. 2.3.6):

$$t = l/u \tag{3.3a}$$

$$\sigma = 2\pi/t \tag{3.3b}$$

$$k = 2\pi/l \tag{3.3c}$$

t is the time it takes for the shear probe to pass an eddy of size l, at the nominal sink velocity U. σ is the corresponding measured frequency, and it is related to the wavenumber k by $\sigma = kU$. Using a fast Fourier transformation (FFT) on half-overlapping 1-second segments of k produces an energy spectrum. Small-scale shear was obtained by iteratively integrating the low wavenumber portion of the shear spectrum, using the equation

$$\overline{\left(\frac{\partial u}{\partial z}\right)^2} = \int_{k_l}^{k_u} \Phi(k)dk, \tag{3.4}$$

where $\Phi(k)$ is the shear spectrum. The choice of upper (k_u) and lower (k_l) wavenumber integration limits are discussed in Fer et al. (2014).

The empirical model for the turbulence spectrum determined by Nasmyth (1970) is used to correct for the variance in the unresolved portions of the spectrum (the noise-affected high wavenumber portion of the spectrum). This study uses the accurate curve fit for the Nasmyth spectrum given in Wolk et al. (2002).

3.1.4 Monthly Isopycnal and Mixed-layer Ocean Climatology (MIMOC)

To compare data collected during the cruise with average conditions, the monthly isopycnal and mixed-layer ocean climatology (MIMOC) is used. MIMOC relies on available quality-controlled profiles of temperature and salinity from the Argo Program, Ice-Thethered Profilers, and from the World Ocean Database (NOAA, 2017). The goal of MIMOC is to present a climatology that is as similar as possible to synoptic surveys in modern time (2007-2011), minimizing transient eddy and wave signatures (Schmidtko

et al., 2013). Available variables from MIMOC is potential temperature, practical salinity, Conservative Cemperature, Absolute Salinity, mixed layer pressure, pressure, mapped year of grid point and sum of raw data weights used for grid points (NOAA, 2017). Data is presented as a global monthly netCDF file with latitude, longitude and pressure coordinates, where the gridding is $0.5° \times 0.5°$. So far, 81 pressure levels between the surface (0 dBar) and 1950 dBar is available, between 80°S and 90°N (NOAA, 2017). MIMOC preserves the surface mixed layer and the density structure, minimizes diapycnal and isopycnal smoothing, and resolves water mass features (Schmidtko et al., 2013).

3.1.5   Arctic Ocean Tidal Inverse Model (AOTIM-5)

The Arctic Ocean Tidal Inverse Model (AOTIM-5) is used to remove the barotropic tide from the current velocity profiles. AOTIM-5 is a high-resolution, 5 km $\times$ 5 km, inverse model of the Arctic Ocean tides (Padman, 2004). An inverse model is a model where the observed behavior is used as an input to find the action causing the behavior. In the case of AOTIM-5, observed data from tide gauges (device for measuring changes in sea level), are used to estimate the volume flux of water needed to cause the observed sea level change. Data from coastal and benthic tide gauges, and data from TOPEX/Poseidon and ERS altimetry are used in the AOTIM-5 for improvements on the four dominant tidal constituents M_2, S_2, K_1 and O_1 (Padman, 2004). M_2 and O_1 are the main lunar semidiurnal and diurnal constituents respectively. S_2 is the main solar semidiurnal constituent. K_1 is the daily declination tide from moon and sun. AOTIM-5 uses bathymetry data from the International Bathymetric Chart of the Arctic Ocean (IBCAO) (Padman, 2004). IBCAO is described below.

3.1.6   International Bathymetric Chart of the Arctic Ocean

The bathymetry data in the study region is gathered from the International Bathymetric Chart of the Arctic Ocean (IBCAO). IBCAO contains all available bathymetry data north of 64°N, and uses a gridding algorithm to provide data for every 0.5 km $\times$ 0.5 km (Jakobsson et al., 2012). The IBCAO data can be downloaded as a netCDF file with latitude and longitude coordinates.

3.2 Methods

3.2.1 Conservative Temperature (Θ) and Absolute Salinity (S_A)

In situ temperature, T, and practical salinity, S, are converted to Conservative Temperature, Θ, and Absolute Salinity, S_A. Conservative temperature is commonly being used as the standard unit in the oceanographic community, instead of potential temperature. For both potential temperature and Conservative Temperature, one imagines that a water parcel at an arbitrary pressure in the ocean is moved in an adiabatic and isohaline manner to the surface pressure $P = 0$ dbar. The potential temperature is the new temperature due to the change in pressure. Conservative Temperature however, is potential enthalpy divided by the fixed heat capacity of the water parcel (McDougall and Barker, 2011). Enthalpy is the total heat content of a system, and so, potential enthalpy is the new enthalpy due to the change in pressure when a water parcel is moved to the surface pressure.

The difference between potential temperature and Conservative Temperature is normally less than 0.1°C in the ocean, however, the difference may be as large as 1.4°C in warm, fresh water (McDougall and Barker, 2011).

Absolute Salinity is salinity in units [g/kg], that is grams of salt per kilogram of water. Practical salinity has no units and is measured on the practical salinity scale, which is defined from the electrical conductivity of salty water. Absolute Salinity is used throughout this thesis. For reference, S_A of $S = 35$, $P = 0$ dbar at 80°N and 10°E is 35.167 g/kg.

The conversion from in situ temperature and practical salinity to Conservative Temperature and Absolute Salinity is done using the Gibbs-SeaWater (GSW) Oceanographic toolbox, described by McDougall and Barker (2011).

3.2.2 Correcting for the tidal currents

The LADCP and VMADCP (section 3.1.2 and 3.1.2, respectively) provided vertical profiles with the u and v components of the ocean currents at specific time and position. The inverse tidal model, AOTIM-5 (section 3.1.5), was used to correct for barotropic tidal currents in the velocity components. The AOTIM-5 model gives the volume flux $[m^2/s]$ at specified latitude and longitude coordinates, for specified times. To find the barotropic tidal current, the volume flux is simply divided by the water depth at that specific location. The water depth is provided by the IBCAO database (see section 3.1.6). At CTD/LADCP stations, where station depth is accurately measured, the volume flux is divided by the station depth, which is considered to be more accurate than

the water depth provided by IBCAO, particularly over steep slopes. The barotropic tidal current components, predicted at the given location and time, are simply subtracted from the velocity components measured by the ADCPs. The time used in the model is always the mid-time of the current profile.

3.2.3   Gridding

Linear Interpolation

The stations along sections A, B and C (see figure 3.1) are not evenly distributed in space, with stations closer together across the continental slope than on the continental plain and shelf. For calculations it is useful to grid the data evenly in space, both in horizontal and vertical. A linear interpolation method is used. The linear interpolation method keeps the original data at their original coordinates.

Conservative Temperature, Θ, Absolute Salinity, S_A, and current profile data from the LADCP, are all linearly interpolated to form a data grid along section A, B and C with 1 km horizontal, and 2 m vertical resolution.

After uniformly gridding the data, a moving average smoothing was performed using a 10 km $\times$ 10 m (horizontal $\times$ vertical) smoothing window. The goal is to look at geostrophic currents, hence, the smoothing is intended to remove ageostrophic variability, and short time/length scale variability, such as internal waves.

Objective interpolation

Whereas the linear interpolation weighs all the observed data points as equally important, an objective analysis is a form of interpolation where the observed data points are more important the closer they are to the gridded points. As with the linear interpolation method, the goal is to interpolate data from unevenly spaced locations onto a fixed grid. That is, we construct a grid of a scalar variable, $D(x,y,z,t)$, from irregularly spaced measurements, $d(x,y,z,t)$, where the measurements include an error, $e(x,y,z,t)$, which can be measurement noise, high frequency variability etc (Thomson and Emery, 2014, ch. 4.2). This yield the equation

$$d(x,y,z,t) = D(x,y,z,t) + e(x,y,z,t). \tag{3.5}$$

The advantage of objective interpolation is that it produces a smoothed version of the original data, removing noise and small scale variations, however, it will also underestimate the true field.

In order to determine how the observed data points will be weighted, one decides on a correlation length. A correlation length is the length scale at which the measured

point's deviation from the mean is correlated. That is, one assumes that the interpolated point at a specified length away from the measured point, does not deviate from the true mean more than the measured point does. For this study, the horizontal correlation length was set to 50 km, and a 5% error was allowed for.

Next, a covariance matrix, $C(r)$, is generated using a Gaussian correlation function,

$$C(r_x, r_y) = (1 - e)\exp(-(x/r_x)^2 - (y/r_y)^2), \qquad (3.6)$$

where e is the allowed error, and r_x and r_y are the longitudinal and latitudinal correlation lengths, respectively. At places where one has no data, one relies on the correlation function. The further away from the data, the more uncertain the fit will be. An error variance field is produced, showing the error associated with each optimally interpolated value. When the error variance exceeds a specific threshold value (% of the total variance) the interpolated data point is untrustworthy. For this thesis, the threshold value is given in the caption of the figures where the objective analysis method is used.

3.2.4 Geostrophic Velocity

The West Spitsbergen Current is known to be a homogeneous current, in which the potential vorticity is conserved. The current follows the f/h contours as it flows northward, where f is the Coriolis parameter, and h is the depth of the water column. The simplest representation of the WSC is a geostrophic flow, where the current is forced by a balance between pressure gradients and the Coriolis acceleration. In a system where the Coriolis term strongly dominates the acceleration terms, looking at long time scales, and neglecting friction, the governing equations reduce to:

$$-fv = -\frac{1}{\rho_0}\frac{\partial p}{\partial x} \qquad (3.7a)$$

$$+fu = -\frac{1}{\rho_0}\frac{\partial p}{\partial y} \qquad (3.7b)$$

$$0 = -\frac{1}{\rho_0}\frac{\partial p}{\partial z} \qquad (3.7c)$$

$$\frac{\partial u}{\partial x} + \frac{\partial v}{\partial y} + \frac{\partial w}{\partial z} = 0 \qquad (3.7d)$$

(Cushman-Roisin and Beckers, 2011, ch. 7.1). The simplified continuity equation 3.7d is a result of applying the Boussinesq approximation $\rho = \rho_0 + \rho'(x, y, z, t)$, where $|\rho'| \ll \rho_0$, on the equation for conservation of mass.

Based on the CTD data (see section 3.1.1), the dynamic height is calculated relative to a reference pressure of 100 dbar, for sections A, B and C in figure 3.1. The dynamic hight is calculated from Absolute Salinity, S_A, Conservative Temperature, Θ, and pressure, P, and is the depth of water parcels relative to the reference pressure.

The dynamic height anomaly is then calculated relative to isobaric surfaces, and becomes the geostrophic stream function. The reference pressure is chosen so that it is away from frictional boundary layers, where ageostrophic currents can be substantial. The relative geostrophic velocity components u and v can be calculated from equation 3.7a and 3.7b, where the Coriolis parameter is $f = 2\Omega \sin \varphi$, Ω is the rotation speed of the Earth in radians per second, and φ is the latitude. The pressure gradients are calculated from the dynamic height anomaly. Dynamic height anomaly and geostrophic velocity are calculated using the GSW Oceanographic toolbox (McDougall and Barker, 2011).

The relative geostrophic velocity is zero at the reference pressure, and all other velocities are relative to that. To calculate the absolute geostrophic velocity, the observed velocity at the reference pressure (detided LADCP data) is simply added to the relative velocities in the entire water column.

3.2.5   Streamtube

When calculating the downstream change in the WSC properties, defining a streamtube, or boundaries of the WSC, becomes essential. Here the WSC streamtube is defined as Atlantic Water ($S_A > 35.05, \theta \geq 2°$C) with absolute geostrophic current velocities higher than 0.04 m/s. The latter is imposed to ensure a dynamic core with measurable horizontal velocity larger than the ADCP error, which is typically a few cm/s.

Mean properties within the streamtube

Average properties within the streamtube are calculated using the arithmetic mean, as well as a weighted mean using the cross section velocity. Equation 3.8 shows the method used to calculate the mean Conservative Temperature weighted with the cross section velocity u, $\overline{\Theta_u}$,

$$\overline{\Theta_u} = \frac{\sum_{i=1}^{n} u_i \Theta_i}{\sum_{i=1}^{n} u_i}, \tag{3.8}$$

where n is the number of data points within the streamtube.

WSC core

The core of WSC (on the horizontal plane) is found by calculating the vertical mean (within the streamtube) of the cross section velocity, for each kilometer along the section. The WSC core is defined as the location where the vertical mean of the cross section velocity is highest, and is marked as $x = 0$ in the different section plots.

3.2.6 Rossby radius of deformation

In a stratified, rotating fluid the dynamical importance of the stratification and rotation are given by the Froude number, Fr, and the Rossby number, Ro, respectively. The following theory and equations are based on the textbook by Cushman-Roisin and Beckers (2011, ch. 11.6 and 12.2).

$$\text{Fr} = \frac{U}{NH}, \tag{3.9}$$

$$\text{Ro} = \frac{U}{\Omega L}. \tag{3.10}$$

Stratification and rotation are important when their respective numbers are on the order of unity or less. The Rossby number compares the distance a fluid parcel with speed U travels horizontally during one Earth revolution (U/Ω) with the typical length scale over which the motion takes place (L). The Froude number compares the horizontal distance a fluid parcel travels during one "buoyancy revolution" (U/N) with the typical layer thickness over which the motion takes place (H). N is the buoyancy frequency, where

$$N^2 = -\frac{g}{\rho_0}\frac{d\rho}{dz} \simeq \frac{g}{\rho_0}\frac{\Delta\rho}{H} = \frac{g'}{H}, \tag{3.11}$$

and g' is the reduced gravity defined as $g' = g\,\Delta\rho/\rho_0$. The relative importance of rotation versus stratification is given by the Burger number,

$$\text{Bu} = \left(\frac{Ro}{Fr}\right)^2 = \left(\frac{NH}{\Omega L}\right)^2. \tag{3.12}$$

When the Burger number is unity, that is, when the effect of stratification and rotation is equally important, a special horizontal length scale occurs where

$$L = \frac{NH}{\Omega}. \tag{3.13}$$

Substituting N with equation 3.11 and Ω with the Coriolis parameter $f = 2\Omega\sin\varphi$ yields

$$R = \frac{\sqrt{g'H}}{f}, \tag{3.14}$$

known as the internal radius of deformation. When two different water masses of different density meet, an adjustment will occur (denser fluid flowing beneath lighter fluid). In a fluid where the Burger number is of unity, this adjustment will spread over a distance R. Hence, fronts and accompanying currents will be on the order of the deformation radius, a length scale often referred to as mesoscale in oceanography. Equation 3.14 will be used to calculate the deformation radius in this study.

3.2.7   Mixed layer

Following Peralta-Ferriz and Woodgate (2015), the mixed layer depth is detected as the maximum depth at which the potential density is within $0.1 \, \text{kg/m}^3$ of the best estimate of the surface density. Even though the definition of the mixed layer depth (MLD) is to some extent arbitrary, numerous different definitions often yield similar results and can confound inter-comparisons of different studies. Peralta-Ferriz and Woodgate (2015) analyzed 21,406 hydrographic profiles collected between 1979 and 2012, and found that their definition gave results that primarily identified the shallowest significant step in water properties, and so, agreed well with heuristic assessments of MLD.

3.2.8   Heat Fluxes

Heat budget

The heat budget of a body of fluid can be written as

$$\frac{\partial \bar{q}}{\partial t} + \mathbf{u} \cdot \nabla \bar{q} - \kappa_H \nabla \bar{q} = 0, \tag{3.15}$$

where the change in heat in time $(\partial \bar{q}/\partial t)$ is balanced by the advection of heat $(\mathbf{u} \cdot \nabla \bar{q})$ and the molecular diffusion of heat $(\kappa_H \nabla \bar{q})$, and the overbar indicates a mean over turbulent timescales (Cokelet et al., 2008; Cushman-Roisin and Beckers, 2011, ch. 3.8 and 3.9). The velocity field, $\boldsymbol{u}$, can be written as $\boldsymbol{u} = \bar{\boldsymbol{u}} + \boldsymbol{u}'$. The molecular diffusion of heat is typically small, and neglected compared to the turbulent eddy heat flux. After Reynolds averaging, equation 3.15 becomes

$$\frac{\partial \bar{q}}{\partial t} + \bar{\mathbf{u}} \cdot \nabla \bar{q} + \nabla \cdot \overline{\mathbf{u}'q'} = 0, \tag{3.16}$$

where $\nabla \cdot \overline{\mathbf{u}'q'}$ is the eddy heat flux.

Following the method described by Boyd and D'Asaro (1994) and Cokelet et al. (2008), one can integrate equation 3.16 over a fixed volume, V, to obtain

$$\frac{\partial}{\partial t} \int_V \bar{q} \, dx dy dz = \int_{Surface} (Q + H) \, dx dy - \int_V \bar{\mathbf{u}} \cdot \nabla \bar{q} \, dx dy dz, \tag{3.17}$$

where Q and H are the heat flux to the atmosphere and sea ice respectively, and it is assumed that only heat flux through the surface is important. Assuming that the local heat content does not change, that is, $\frac{\partial}{\partial t} \int_V \bar{q} \, dx dy dz = 0$, the surface heat flux must balance the divergence of heat. The heat content in a body of fluid, $\bar{q}$, is given by

$$\bar{q} = \rho_0 C_P \bar{T} \tag{3.18}$$

where ρ_0 is the density, C_P is the specific heat capacity of seawater, and $\bar{T}$ is the mean temperature. Substituting $\bar{q}$ in equation 3.17 with equation 3.18, and assuming that the

velocity field, $\boldsymbol{u}$, consists of only a northward velocity, v, and applying Gauss's theorem on the volume integral of the heat advection, yield

$$\int_{Surface} (Q + H) \, dxdy = \rho_0 C_P \bar{v} \frac{\partial}{\partial y} \int_A \bar{T} \, dxdz, \qquad (3.19)$$

where A is the area of the current's cross section.

From equation 3.19, the surface heat loss per meter northward (W m^{-1}) above WSC can be estimated by knowing the mean current velocity, $\bar{v}$, the northward temperature gradient, $\partial \bar{T}/\partial y$, and the current cross section area, A. This study uses Conservative Temperature in the calculations. For surface heat flux (W m^{-2}), the heat loss from equation 3.19 is divided by the width of the current (streamtube).

Vertical heat flux from microstructure profiles

Direct measurements of the heat flux, $\overline{w'T'}$, are very demanding on the instrumentation, hence the vertical heat flux, due to turbulent motion, is often expressed as

$$\overline{w'T'} = -K_T \frac{d\bar{T}}{dz}, \qquad (3.20)$$

where T' is the temperature fluctuations from the mean temperature, $\bar{T}$, w' is the vertical velocity fluctuations at which the temperature variations are carried, $d\bar{T}/dz$ is the vertical temperature gradient, and the parameter K_T is the eddy diffusivity coefficient of heat (Thorpe, 2007, ch. 2.2.2). The eddy diffusion of heat relates to the molecular diffusion of heat, κ_H, in the following way:

$$K_T = \kappa_H C, \qquad (3.21)$$

where C is known as the Cox number, and in an isotropic field (see section 3.1.3) the Cox number is given as,

$$C = \frac{3 \overline{\frac{\partial T'}{\partial z}^2}}{\overline{\frac{d\bar{T}}{dz}}^2} \qquad (3.22)$$

(Thorpe, 2007, ch. 4.4.2). In practice, K_T can then be measured using a free-fall instrument that measures the vertical variations of ocean temperature, however, this method also places severe demands on the instruments, demanding resolution of very small variations in temperature.

A standard method to estimate the eddy diffusivity coefficient of heat is to assume that heat and density diffuse with similar coefficients in a turbulent flow, that is, $K_T \approx K_\rho$, where K_ρ is the diapycnal eddy diffusivity coefficient. The eddy diffusivity coefficient is readily obtained from shear probe data as,

$$K_\rho = \Gamma \frac{\varepsilon}{N^2}, \qquad (3.23)$$

where Γ is the "efficiency factor", ε is the turbulent dissipation, and N is the buoyancy frequency (Thorpe, 2007, ch. 4.4.2). Equation 3.23 comes from assuming that the ocean within the study region is in a steady state, that is, the turbulent energy does not change over time. The efficiency factor, Γ, is commonly set to 0.2, even though the exact value may differ from this (Thorpe, 2007, 4.4.2). The heat flux is ultimately calculated from the shear measurements, substituting equation 3.2 and 3.23 into equation 3.20.

4 | Results

4.1 Hydrography and Water masses

Figure 4.1 shows the Conservative Temperature and the Absolute Salinity along the three CTD sections A, B and C, including the streamtubes defined in section 3.2.5 Note that section A is the northern most section, and C is the southernmost section. For each section, the upper panel shows Conservative Temperature, Θ, while the lower panel shows Absolute Salinity, S_A. The horizontal distance is referenced to the location of the geostrophic velocity peak in each section. For all three sections, the warmest and freshest water was found at the surface, with temperatures up to 8°C, and salinities down to below $25 \, \mathrm{g \, kg^{-1}}$. In general, the temperature decreases with depth, and is about -1°C at the deepest stations. The salinity increases down to 50 m, where it remains above $35.2 \, \mathrm{g \, kg^{-1}}$ down to about 400-m depth, and decreases with depth below 400 m. Figure 4.2 shows the potential density profiles for the upper 60-m at the different sections. The profiles are color coded according to the depth of the station. Blue is on the seaward side of the defined streamtube, red is within the streamtube, while green is on the landward side of the streamtube. Figure 4.3 shows the water masses found in each section, where black lines show the streamtubes. The different water masses are described in table 2.1. Figure 4.4 shows the temperature-salinity-diagrams for the different sections. Next follows an individual description of the hydrography in each section.

4.1.1 Hydrography along section A

Section A is the northernmost section, stretching approximately 49 km in a north-south direction (see figure 3.1). The northernmost station (A13) is at 80°41.86′N and 12°29.63′E, at 1317 m depth. The southernmost station (A1) is at 80°15.66′N and 12°29.65′E, at 184 m depth. In figure 4.1a, upper panel, a tongue of warm water stretches downward between -5 and 0 km, just north of the continental shelf, marking the location of the inner branch of the WSC. The warm tongue ($\Theta > 2°C$) extends seaward in a 400-m thick layer, with colder water intruding above it at 50 m depth.
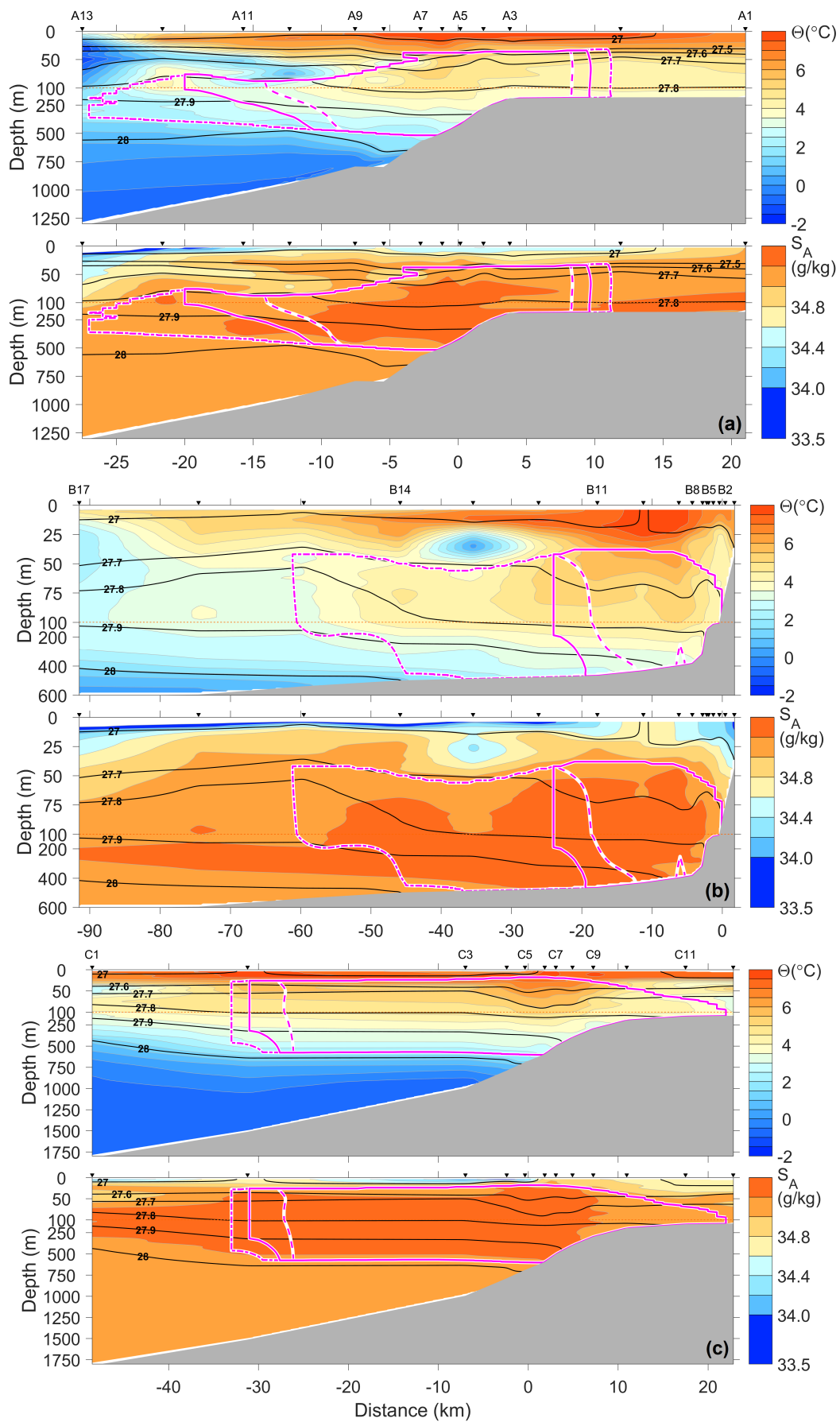
Figure 4.1 - See caption on next page.

Figure 4.1 – (On the left) CTD sections. Top panel in each figure is Conservative Temperature (Θ), while bottom panel is Absolute Salinity (S_A). The color bar for temperature has color intervals at every 0.5°C. The color bar for salinity has interval from 33.5 g kg^{-1} to 34.0 g kg^{-1}, then at every 0.2 g kg^{-1}. Black lines are density lines. Solid magenta line shows the defined streamtube (see section 3.2.5), where the dashed line is the inner error estimate and the dot/dashed line is the outer error estimate. Note, the depth scale on the y axis and the distance on the x axis varies from section to section. The upper 100 m of each section has a different scale than the lower part, separated with a dashed red line.
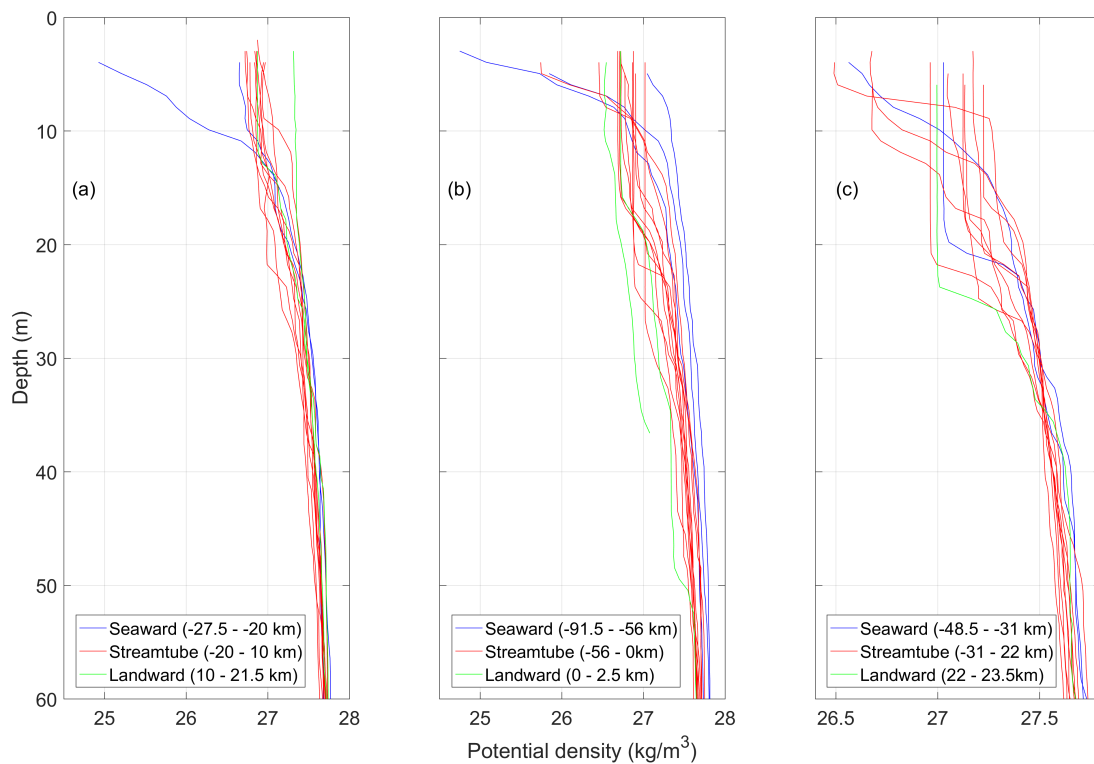
Figure 4.2 – Potential density profiles of the upper 70 m. Section A, B and C are shown from left to right. Blue lines are the density profiles on the seaward side of the streamtube, that is, over the deepest part of the section. Red lines are the profiles through the streamtubes. Green lines are the profiles landward of the streamtubes, over the shallowest part of the section. The distance in the legends correspond to the distance on the axis in figure 4.1.

(a) Section A

(b) Section B
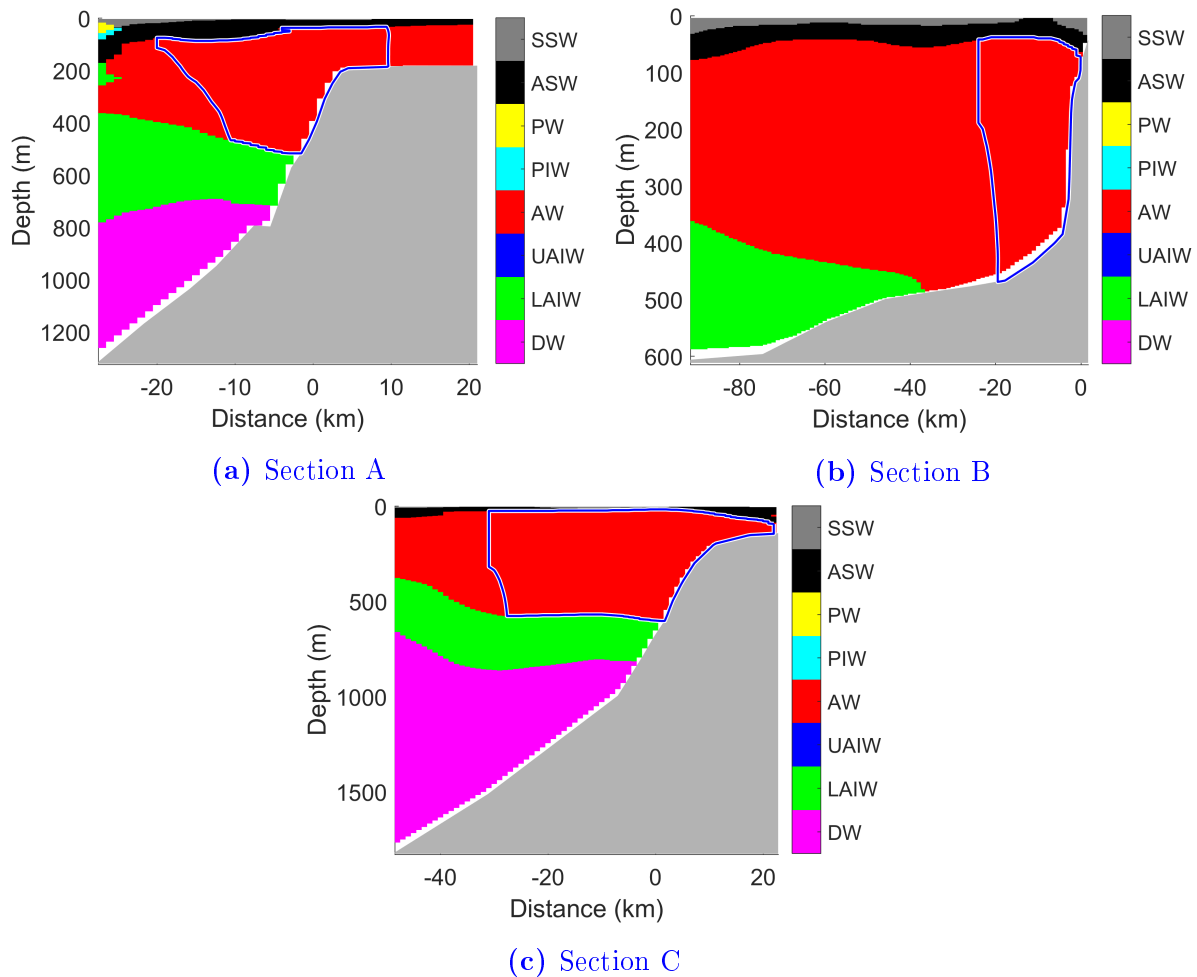
(c) Section C

Figure 4.3 – Water masses found in section A, B and C, as defined in table 2.1. The different water masses are; summer surface water (SSW), Arctic surface water (ASW), polar water (PW), polar intermediate water (PIW), Atlantic water (AW), upper-Arctic intermediate water (UAIW), lower-Arctic intermediate water (LAIW), and deep water (DW). The area enclosed by the blue line in each section is the defined streamtube (see section 3.2.5). Note, the vertical and horizontal scale differ from section to section.

(a) Section A

(b) Section B

(c) Section C

Figure 4.4 – Temperture-salinity diagram for section A, B and C. Dashed red lines are Gade lines as described in figure 2.3. The black boxes indicate the different water masses as described in table 2.1. The black dots indicate water in the upper 100 m of the water column, re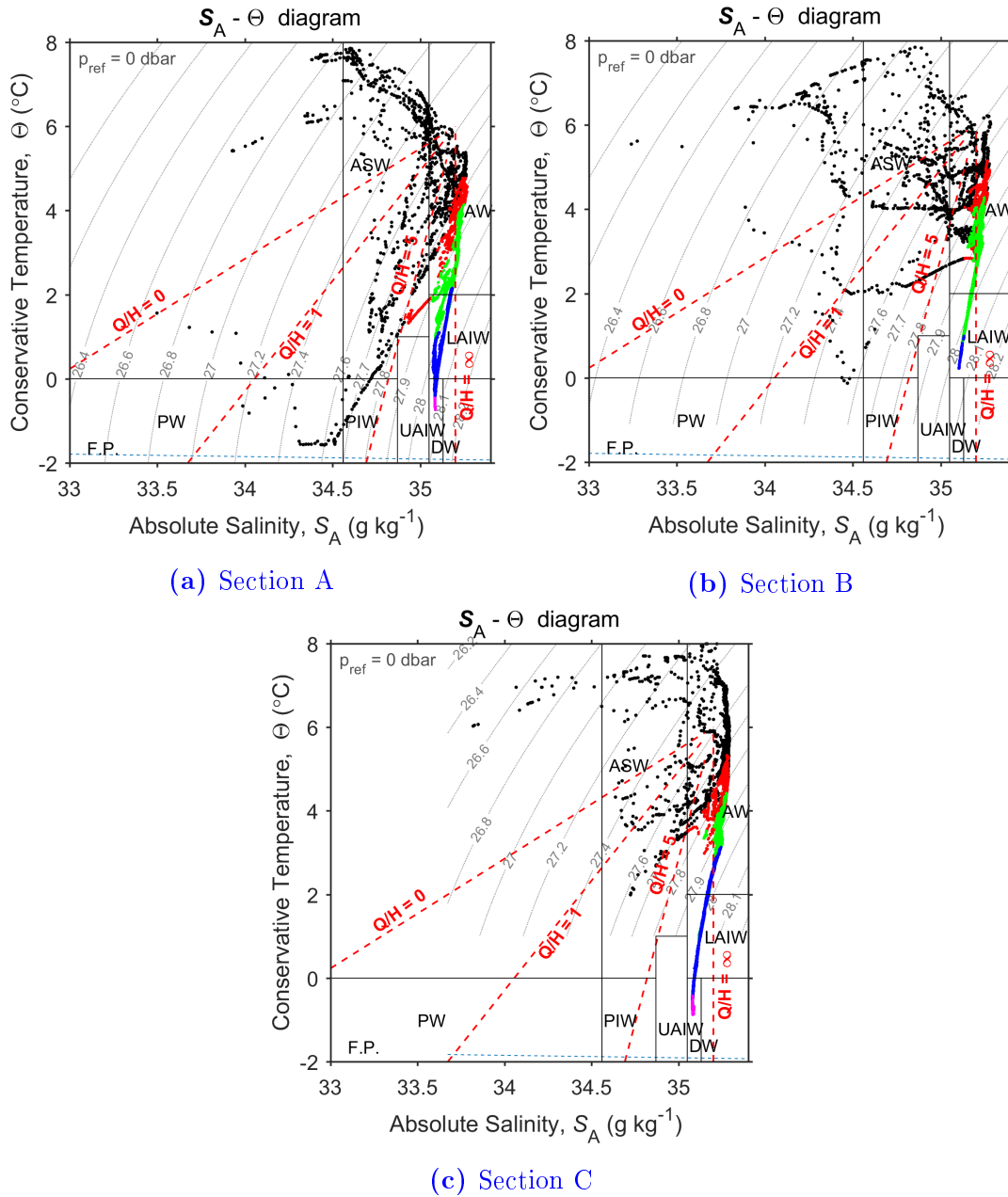d indicates 100 to 200m, green indicates 200 to 500 m, blue indicates 500 to 1000 m, and magenta indicates water deeper than 1000 m.

Between -22 and -12 km, at 80 m depth, a pattern resembling an eddy can be seen. From equation 3.14, the deformation radius calculated between the 27.6 kg m^{-3} and 28 kg m^{-3} isopycnals, for a 450 m thick layer at 80.5°N, is 9 km, consistent with the horizontal length scale of the feature. In the lower panel of figure 4.1a, water of salinity higher than 35.2 g kg^{-1} is located at 0 km, between 50 m and 500 m depth, with a tongue stretching seaward, and a tongue of fresh water intruding above it. The same eddy like pattern is present in the salinity profile as in the temperature profile. At station A13, remnants of a cold halocline layer is present, with fresh melt water at the surface, cold temperatures reaching down to 50 m depth, and well stratified in salinity. The 27 kg m^{-3} isopycnal outcrops at 14 km.

Figure 4.2a shows the potential density profile of the 13 different stations along section A. The mean mixed layer depth, defined as the maximum depth at which the potential density is within 0.1 kg m^{-3} of the surface density, is 11 m, with a standard deviation of 5 m. The mixed layer depth for the different stations ranges between 4 and 22 m, with a tendency of deeper mixed layers towards shallower depths.

The different water masses found in section A can be seen in figure 4.3a. At station A13 (-27.5 km) , summer surface water (SSW) overlays polar water (PW), polar intermediate water (PIW), and Arctic surface water (ASW). From figure 4.4a it is clear that the formation of the PIW and the PW follows a Gade line equivalent to a slope between Q/H = 0 and Q/H = 1. That is, the PW and the PIW is formed from Atlantic water (AW) when heat lost to sea ice is a major heat sink. Also the small part with lower Arctic intermediate water (LAIM) above AW seems to come from AW being cooled by melting of sea ice. LAIW and deep water (DW) below the AW follows a Gade line similar to Q/H = 5, suggesting heat lost to the atmosphere is the major transformer.

4.1.2   Hydrography along section B

Section B is the section toward the Yermak Plateau. It consists of 17 stations, stretching approximately 94 km in a northwest-southeast direction, oriented 49° counterclockwise from north (see figure 3.1). The northern most station (B17) is located at 80°21.04′N and 6°53.68′E, at 607 m depth. The southern most station (B1) is located at 79°48.07′N and 10°33.07′E, at 46 m depth. In figure 4.1b, upper panel, warmest water is located at the surface near the -10 km mark, where the 27 kg m^{-3} isopycnal outcrops. The temperature decreases with depth, and also seaward. At the bottom of station B17, the temperatures drop below 1°C. The coldest temperatures are found at station B13, at 35 m depth, where a pocket of cold ($\Theta = -0.1°C$) and relatively fresh ($S_A = 34.3$ g kg^{-1}) water is located. In general in section B, the sea water is freshest at the surface (lower panel of figure 4.1b) with salinities down to 31.25 g kg^{-1} on the seaward side.

The major body of section B has salinities above 35.2 g kg^{-1}.

Figure 4.2b shows the potential density profile of the 17 different stations along section B. The mixed layers ranges between 3 and 29 m. The deepest mixed layers are found at stations B10, B9 and B8, where the depth of the mixed layer is 29 m, 25 m and 22 m respectively. The mean mixed layer is 13.5 m, with a standard deviation of 7.5 m.

Figure 4.3b shows the water masses found in section B. SSW overlays ASW, except at -10 km, where ASW outcrops (station B10). AW occupies most of the water column between 70 and 450 m depth, overlaying LAIW. From figure 4.4b it is clear that atmospheric cooling has been the main transformer in the production of LAIW, however, events of ice melt have transformed some AW into ASW.

4.1.3   Hydrography along section C

Section C is the southernmost section, stretching over 72 km in a west-east direction (see figure 3.1). The westernmost station (C1) is located at 79°17.96′N and 5°32.78′E, at 1822 m depth. The easternmost station is located at 79°18.03′N and 9°0.19′E, at 145 m depth. Figure 4.1c shows a contour plot of the Conservative Temperature and Absolute Salinity along section C. The temperature is highest at the surface, with temperatures up to 8°C, decreasing with depth. The warm water reaches deeper over the continental slope, near 0 km, then it does elsewhere, marking the location of the WSC. Near station C1, at 50 m depth, colder water intrudes above warmer water. The coldest water is found at depth, where temperatures approach -1°C. The lowest salinity water is found at the surface with salinities down to 33.82 g kg^{-1}, however, most surface salinities are above 34.4 g kg^{-1}, and at station C7, salinities above 34.8 g kg^{-1} outcrop at the surface. The 27 kg m^{-3} isopycnal outcrops at station C2, and from stations C6 to C10. Highest salinities are found between 50 m and 500 m depth.

Figure 4.2c shows the potential density profile of the 12 different stations along section B. The mean mixed layer depth along section C is 16 m, with a standard deviation of 6.5 m. The mixed layer ranges between 5 m and 24 m, with the deepest mixed layers found at stations C11 and C12, where they were 22 m and 24 m respectively. The third deepest mixed layer was 21 m, found at station C2.

In figure 4.3c, showing the water masses along section C, SSW is nearly absent, and ASW is on top of AW. From figure 4.4c, it is clear that SSW and ASW is produced along Gade lines comparable to Q/H = 0, suggesting AW has melted sea ice. LAIW is produced along a Gade line comparable to Q/H = 5, suggesting that heat lost to the atmosphere is the main transformer. DW follows a Gade line where Q/H = ∞, suggesting that heat lost to the atmosphere is the only transformer. The AW layer

is thicker near the continental slope than over deep water. Both LAIW and DW are higher in the water column at station C1 than in the rest of the section.

4.2   Currents

4.2.1   Current structure along section A

Figure 4.5-Section A shows calculated absolute geostrophic velocity (figure 4.5a), and current measurements from the LADCP (figure 4.5b) and the VMADCP (figure 4.5c) for section A. The geostrophic velocity is perpendicular to the section. LADCP and VMADCP data are presented as the along and across section components. In section A u is eastward component and v is northward component.

In figure 4.5a the geostrophic structure forms a rapid flowing barotropic current just seaward of the continental shelf in section A. This is recognized as the inner core of the WSC. The geostrophic velocity exceeds 0.28 m/s at the center of the current (positive velocities are into the paper). On the southern side of the section (on the shelf), the geostrophic structure shows a current exceeding 0.12 m/s flowing in the opposite direction (out of the paper).

Detided current measurements from the LADCP and the VMADCP are shown in figure 4.5b and 4.5c. The upper panel in each figure shows the eastward (u) component, and it is clear that the measured current has a structure very similar to that of the geostrophic velocity. The highest eastward velocity measured by the LADCP exceeds 0.32 m/s, whereas the highest velocity measured by the VMADCP exceeds 0.36 m/s. Between -25 and -17 km   (between station A13 and A11), the current structure support

Figure 4.5 – (Next page) Geostrophic velocity and current measurements for section A, B and C. Geostrophic velocity is the top figure in each section, figure (a), (d), (g). The geostrophic velocity is perpendicular to the section, with positive values going into the paper. Black density lines have been included in the geostrophic velocity plot. LADCP measurements are shown in the middle figure in each section, figure (b), (e), (h). VMADCP measurements are shown in the bottom figure in each section, figure (c), (f), (i). LADCP and VMADCP measurements show u and v components in the upper and lower panel, respectively. In section A, u is perpendicular to the section (eastward) and v is along section (northward). In section B, u is along section (southeast) and v is perpendicular to the section (northeast). In section C, u is along section (eastward) and v is perpendicular to the section (northward). CTD stations are marked along the top axis in the geostrophic velocity and LADCP plots. In the LADCP and VMADCP plots for section A and C, the upper 100 m is in a different scale than the lower part, marked by a dotted red line.
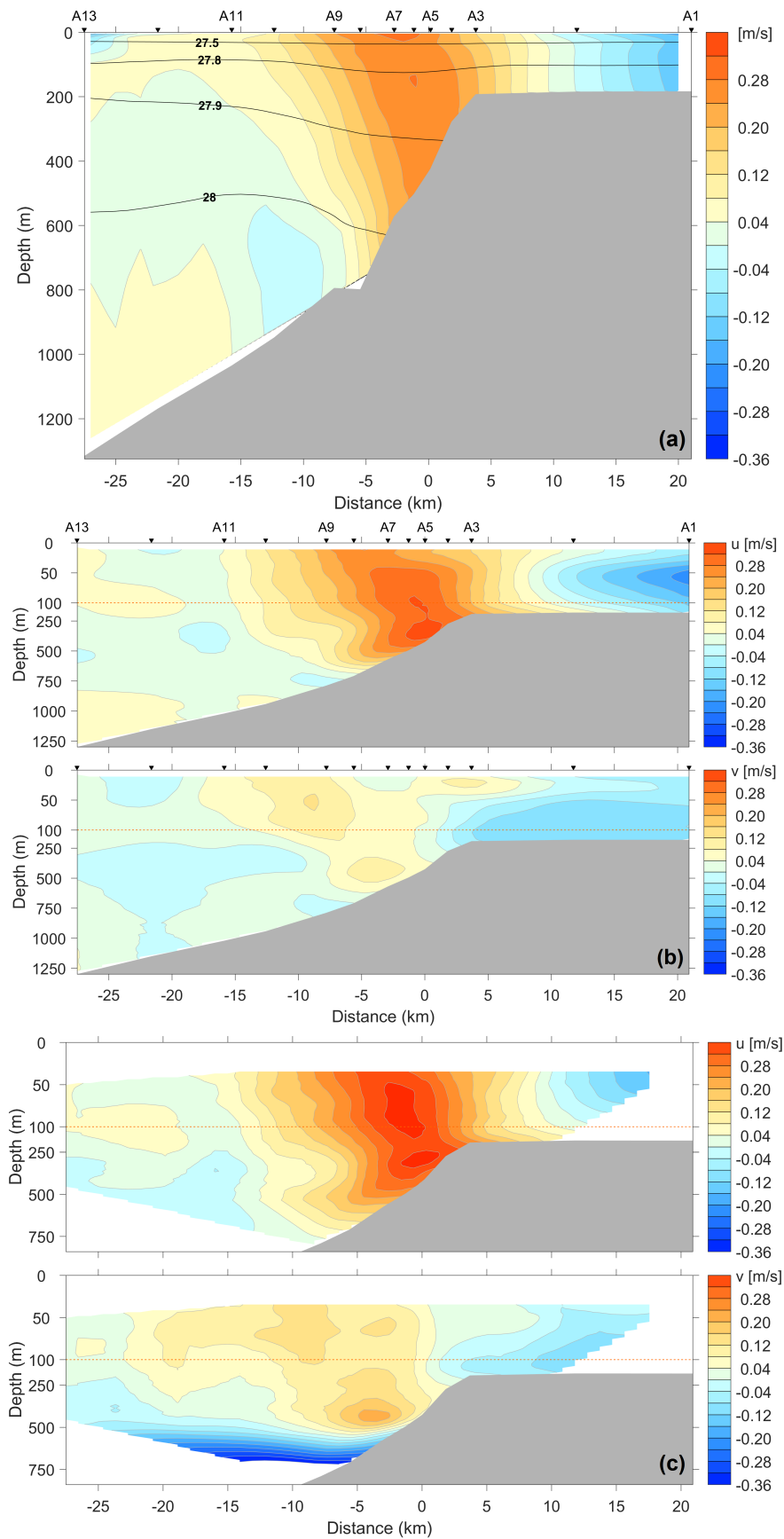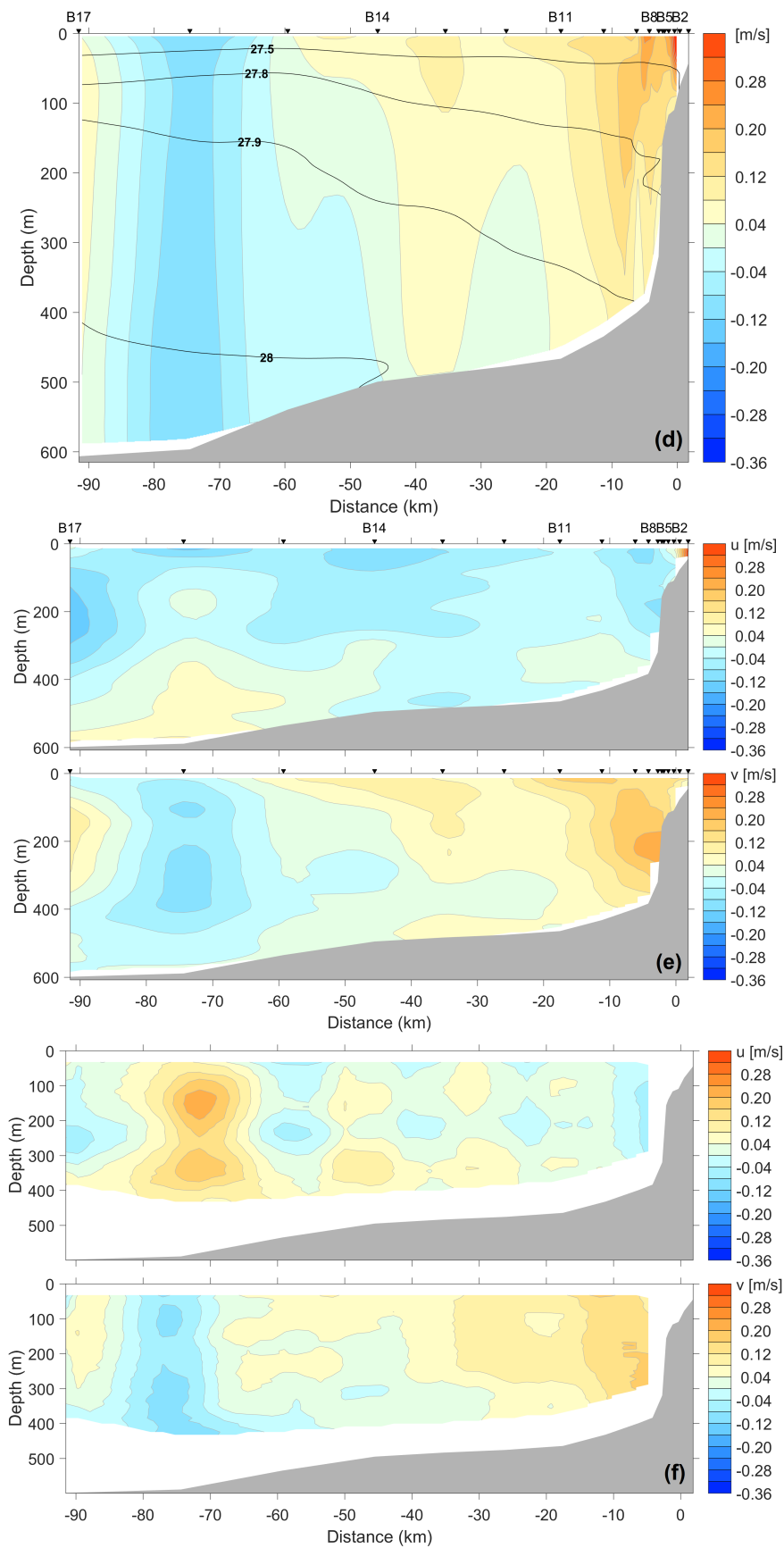
Figure 4.5 – Section A (see caption above)
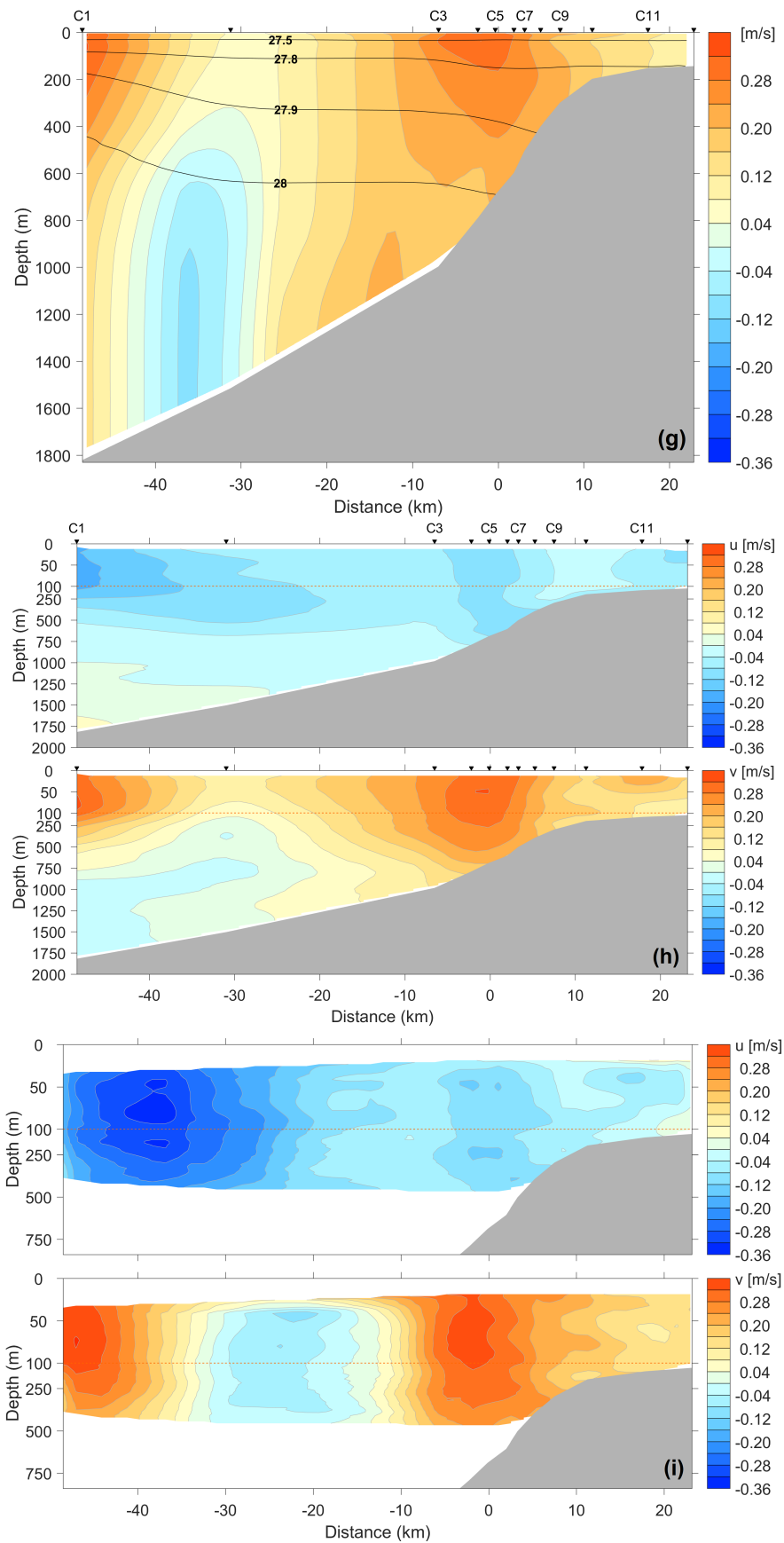
Figure 4.5 – Section B (see caption above)

Figure 4.5 – Section C (see caption above)

the findings presented in section 4.1.1 of an slow, clockwise rotating, eastward moving eddy, at about 80 m depth.

The lower panel in each of figure 4.5b and 4.5c shows the northward component (v). Just at the edge of the continental shelf, the northward component shows a divergence in the flow. North of the shelf, the flow is northward, while it is southward on the shelf. Such a divergence could cause detachments of AW from the WSC, leading to a more efficient cooling.

4.2.2   Current structure along section B

Figure 4.5-Section B shows calculated absolute geostrophic velocity (figure 4.5d), and current measurements from the LADCP (figure 4.5e) and the VMADCP (figure 4.5f) for section B. LADCP and VMADCP data are presented as u and v components. In section B, u and v have been rotated so that u is the along section component and v is perpendicular to the section.

Figure 4.5d shows the geostrophic velocity structure along section B. Between -45 km and 1.5 km the flow is positive (into the paper), with the highest velocities close to the steep slope near 0 km, marking the inner branch of the WSC. Between -85 and -60 km, there is a barotropic flow exceeding 0.08 m/s flowing in the opposite direction of the WSC. The lower panel in figure 4.5e (LADCP) and 4.5f (VMADCP) shows the detided v component, and it is clear that both the LADCP data and the VMADCP data show similar currents as the geostrophic velocity structure. The barotropic current between -85 and -60 km, flowing opposite of the WSC, is too large to be an eddy, but may be a WSC recirculation.

The upper panel in figure 4.5e shows the along section component, where negative numbers are seaward. The LADCP measurements show positive velocities between -80 and -60 km, below 300 depth, elsewhere the currents are mainly seaward. Near the shallowest depths, just before the steepest slope (1 km) the u component from the LADCP measurements show a divergence in the flow. On the shallow side of 0 km, the currents are toward land, while on the deeper side, the currents are towards sea.

The upper panel in figure 4.5f shows the along section component measured by the VMADCP. Between -80 and -60 km the currents are highly positive, exceeding 0.20 m/s. However, there seem to be a spatial signal where the u component alternate between positive and negative currents, and so it may be untrustworthy.

4.2.3   Current structure along section C

Figure 4.5-Section C shows calculated absolute geostrophic velocity (figure 4.5g), and current measurements from the LADCP (figure 4.5h) and the VMADCP (figure 4.5i)

for section A. LADCP and VMADCP data are presented as u and v components. In section C, u is eastward component and v is northward component.

Figure 4.5g shows the geostrophic velocity structure along section C. There are two distinct currents flowing northward along section C. One located on the seaward edge of the section, and one just off the continental shelf, both exceeding 0.28 m/s. Both the LADCP and the VMADCP measurements show the same structure (lower panel of figure 4.5h and 4.5i), however, whereas the inner branch is a mainly barotropic current, the LADCP data show that the outer branch is not barotropic. The outer branch also has a high negative u component (upper panel figure 4.5i) exceeding -0.24 m/s.

The current measurements along section C suggest that parts of the WSC has detached from the inner branch. The inner branch continues to follow the 500 m isobath, while the outer branch does not follow any specific isobath.

4.2.4 Objective analysis of VMADCP data

Figure 4.6 shows an objective analysis of the upper 500 meters of the collected VMADCP data in the region of interest. The VMADCP data are presented as detided vertical means.

Just south of section C, at about 79°5′N and 8°E, a divergence in the flow occurs, splitting the WSC. The divergence is present between the 2000-m isobath and the 200-m isobath, continuing as far north as 79°20′N. Water masses detaching south of 79°20′N flows west, and then north along the outer edge of the Molly Hole described in section 2.1. Just north of 79°20′N, water west of the 1000-m isobath converges with southwestward flowing water continuing towards the Molly Hole. Water east of the 1000-m isobath flows north to 79°35′N where it converges with southeastward flowing waters, and continues over the Yermak Plateau, converging on the landward side of section B, between the 100-m and 400-m isobaths. At 80°10′N and 11°30′E there is a recirculation originating from the divergence on the continental shelf along section A. At 80°5′N and 8°50′E, current measurements suggest the presence of a cyclonic gyre, however, the currents are weak and there are few data points further north. The high southwestward currents found at 80°40′N and 12°E, and continuing southeastward, are likely a result of high correlation length scales (50 km) and few data points.
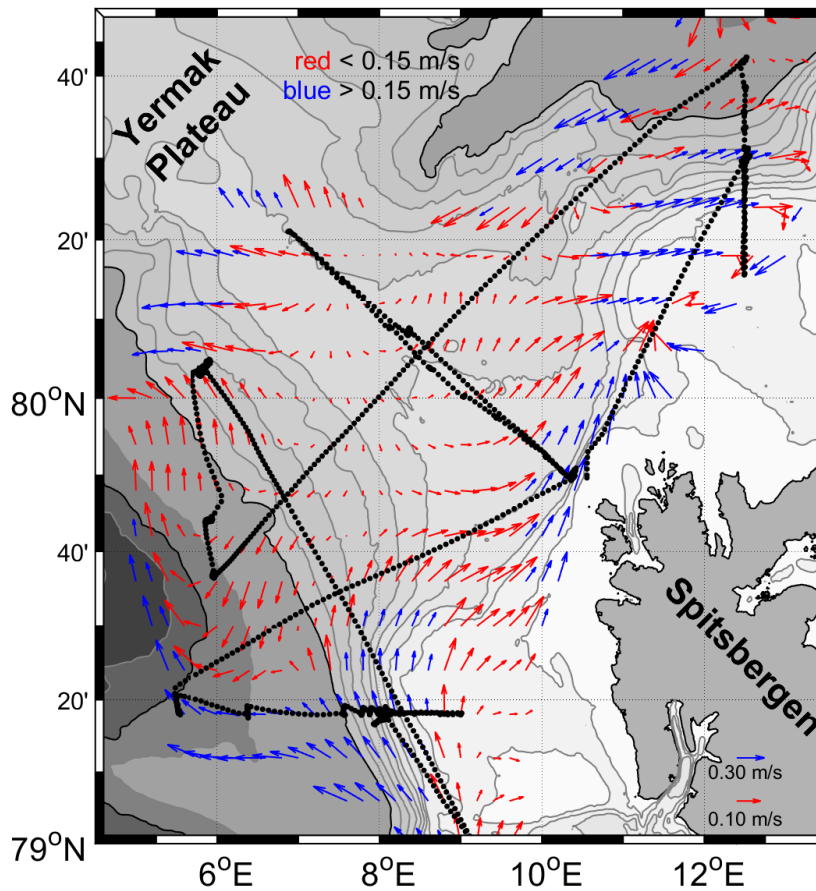
Figure 4.6 – Objective analysis of VMADCP data. Data are presented as detided vertical means in the upper 500 meters, with arrows showing the size and direction of the currents. Red arrows show currents less than 0.15 m s^{-1}, blue arrows show currents higher than 0.15 m s^{-1}. Black dots show the ship track where VMADCP data were collected. Data in the objective mapping exceeding 0.4 m s^{-1} have been removed. Data where the error variance exceeds 5% of the total variance have been removed. Isobath lines are drawn at every 100 m in the upper 1000 m, thereafter for every 500 m.

4.3   Streamtube

Figure 4.7 shows the defined streamtubes in section A, B and C, plotted on geostrophic velocity. The streamtube is defined as Atlantic water ($\Theta > 2°$ C, $S_A > 35.05$ g kg^{-1}) with velocities higher than 0.04 m s^{-1}. LADCP data was used to adjust the calculated geostrophic velocity, in order to get absolute geostrophic velocity. The ADCP error was estimated to be ± 0.03 m s^{-1}, hence an inner (0.07 m s^{-1}) and outer (0.01 m s^{-1}) tube are included, showing the extent of the upper and lower error, respectively. Properties calculated within the streamtube are given in table 4.1 Errors in square brackets show what the difference would be if calculated for the 0.01 m s^{-1} tube (first error), and the 0.07 m s^{-1} tube (second error). In general, the errors between the inner and outer

Table 4.1 – Properties within streamtube A, B and C. The errors listed in square brackets show the difference if values were calculated for an outer streamtube with boundaries at 0.01 m/s (first error), and an inner streamtube with boundaries at 0.07 m/s (second error), including processing errors (see fig. 4.7). If values do not have square bracket errors, it is because the value did not change even if the tube changed. Errors not in brackets are instrumental and processing errors. Whenever errors in square brackets are both positive or both negative, it is because both the inner and outer tube changed the value in the same direction.

	Streamtube A	Streamtube B	Streamtube C
$\mathbf{\Theta}$ (°C), max / min	5.65 [+0.19, -0.02] / 2.00	6.37 / 2.64 [-0.63, +0.41]	7.45 / 2.00
$\overline{\mathbf{\Theta}}$ (°C), arithmetic/ weighted	3.58 [-0.26, +0.11] / 3.65 [-0.08, +0.03]	4.18 [-0.46, +0.22] / 4.22 [-0.30, +0.06]	3.88 [-0.03, +0.07] / 3.91 [0.00, 0.00]
$\mathbf{S_A}$ (g kg^{-1}), max / min	35.240 / 35.051	35.264 / 35.051	35.281 / 35.051
$\overline{\mathbf{S_A}}$ (g kg^{-1}), arithmetic mean / weighted mean	35.186 [-0.005, +0.005] / 35.201 [-0.004, +0.001]	35.211 [-0.006, -0.021] / 35.215 [-0.002, -0.004]	35.206 [0.000, -0.004] / 35.229 [0.000, 0.000]
$\mathbf{v_{ges}}$ (m s^{-1}), max / mean	0.28 ± 0.03 / 0.14 [-0.03, +0.03]	0.23 ± 0.03 / 0.10 [-0.04, 0.00]	0.32 ± 0.03 / 0.17 [0.00, +0.01]
$\mathbf{A}$ (km^2), cross area	8.0 [+3.7, -1.6]	7.7 [+12.4, -2.4]	21.7 [+1.4, -1.8]
$\mathbf{V}$ (Sv), transport	1.1 [+0.2, 0.0]	0.8 [+0.5, -0.3]	3.6 [+0.1, -0.2]
Width (km)	29.7 [+8.5, -7.2]	24.0 [+37.1, -0.3]	53.0 [+2.0, -3.2]
Heat change $\times 10^6$ (W m^{-1})	-7.91 [-8.40, +1.33]	-5.60 [-10.4, +2.37]	-26.2 [-21.2, +5.00]
Bulk $\mathbf{F_H}$ (W m^{-2})	-266 [-160, -26]	-234 [-28, +98]	-494 [-375, +68]
Heat change $\times 10^6$ (W m^{-1}), weighted	-6.97 [-3.56, +0.99]	-4.94 [-5.40, +2.03]	-23.1 [-7.79, +1.90]
Bulk $\mathbf{F_H}$ (W m^{-2}), weighted	-235 [-9, +1]	-206 [+37, +83]	-435 [-126, +10]

tubes are large, due to the fact that the tubes are sensitive to the velocity boundary. The sections are named A, B, C according to the order at which the data was collected during the cruise. however, it is useful to discuss the sections, and how they change, from south to north. Below, the sections will be described in the order C, B, A. Table

4.2 shows the mean northward gradients within the tubes and the mean northward heat loss. Figure 4.8 shows the vertical means of temperature, salinity and geostrophic velocity within the streamtubes.

4.3.1   Streamtube C

The streamtube in section C (figure 4.7c), hereby referred to as streamtube C, has a cross section area of 21.7 [+1.4, -1.8] km^2, and a corresponding mean geostrophic velocity, V_{ges}, of 0.17 [0, +0.01] m s^{-1}. It is the largest streamtube, both in size and volume, and transports 3.6 [+0.1, -0.2] Sv northward. The boundaries of streamtube C are not sensitive to choices of 0.01 m s^{-1} and 0.07 m s^{-1} thresholds (compared to streamtube B and A), and so, the associated errors are relatively small, except for in the heat change calculations. Heat change is calculated from equation 3.19, and uses the northward temperature gradients from table 4.2. The temperature gradient, especially the gradient based on arithmetic mean temperature in each tube, is sensitive to the deformation of the streamtube. The outer tube includes much more cold water than the inner tube, which is clear from figure 4.1a and 4.1b, hence the temperature gradient is much larger following the outer tubes, than it is following the inner tubes. The bulk heat flux in streamtube C is -494 W m^{-2} and -435 W m^{-2}, calculated from the arithmetic mean and weighted mean temperature gradients, respectively. Note, the 0.04 m s^{-1} contour in figure 4.7c continues seaward. There is AW seaward from the tube, and the tube could thus have been extended. However, it is unclear what the outer current is, whether it is an outer branch or potentially due to baroclinic instabilities. The geostrophic velocity plot shows the outer current as a barotropic current, but the LADCP measurements in figure 4.5h show that it is not barotropic. Either way, it is not fully resolved, and this study considers the outer current to be separate from the WSC.

From figure 4.8c, the geostrophic velocity forms a symmetric peak in the middle of the tube. On the landward side (20 km), the temperature and salinity drop rapidly due to fresher and colder shelf waters from Svalbard. On the seaward side the salinity

Figure 4.7 – (Next page) Streamtubes on geostrophic velocity for (a) section A, (b) section B, (c) section C. The 0.04 m s^{-1} streamtube is marked with a solid blue line. The lower ADCP error (-0.03 m s^{-1}) is marked with an outer blue, dashed line along the 0.01 m s^{-1} boundary. The higher ADCP error (+0.03 m s^{-1}) is marked with an inner blue, dashed line along the 0.07 m s^{-1} boundary. The magenta lines show density lines between which microstructure measurements are averaged (section 4.5). Note, from south to north, the order of the figures are (c), (b), (a).
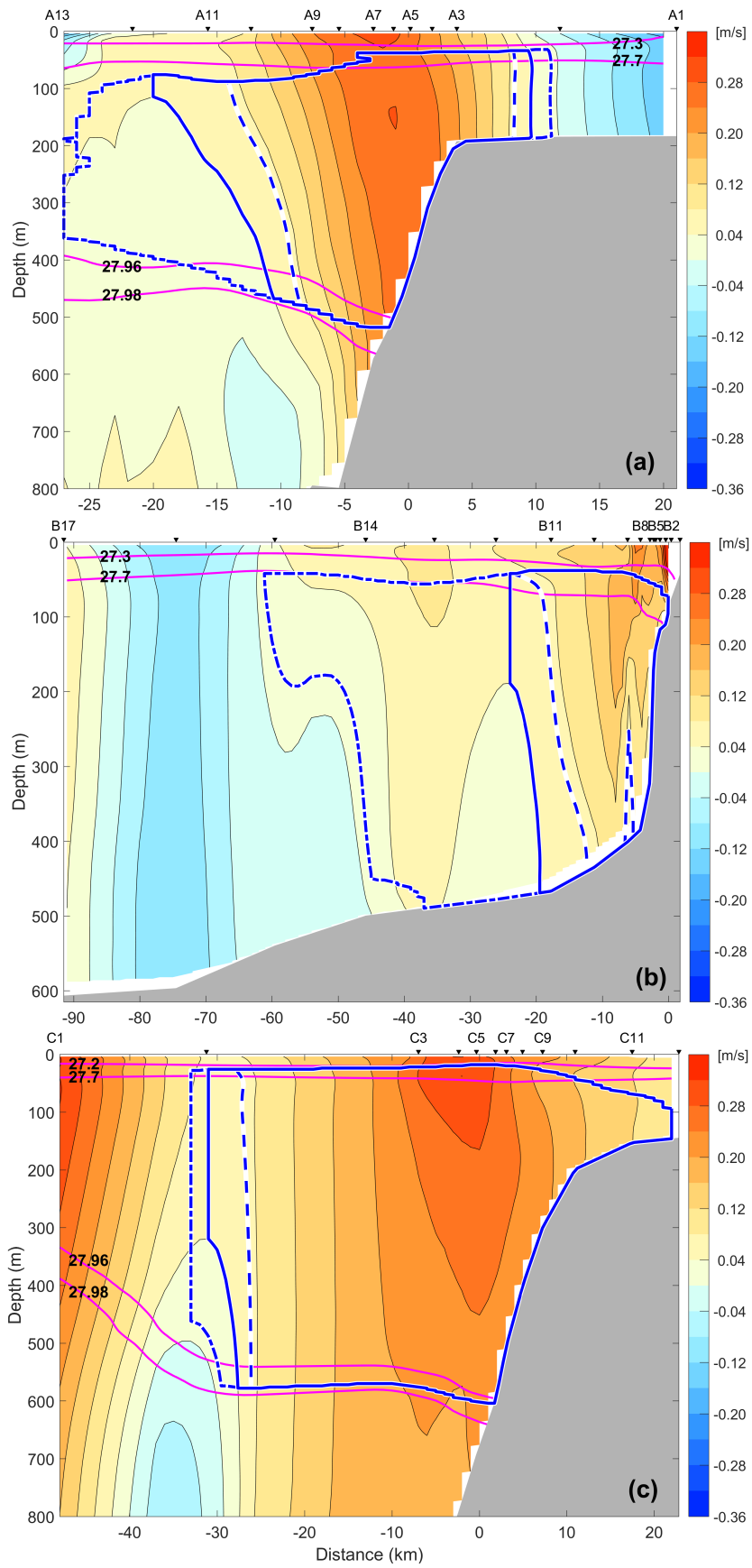
Figure 4.7 - See caption on previous page.
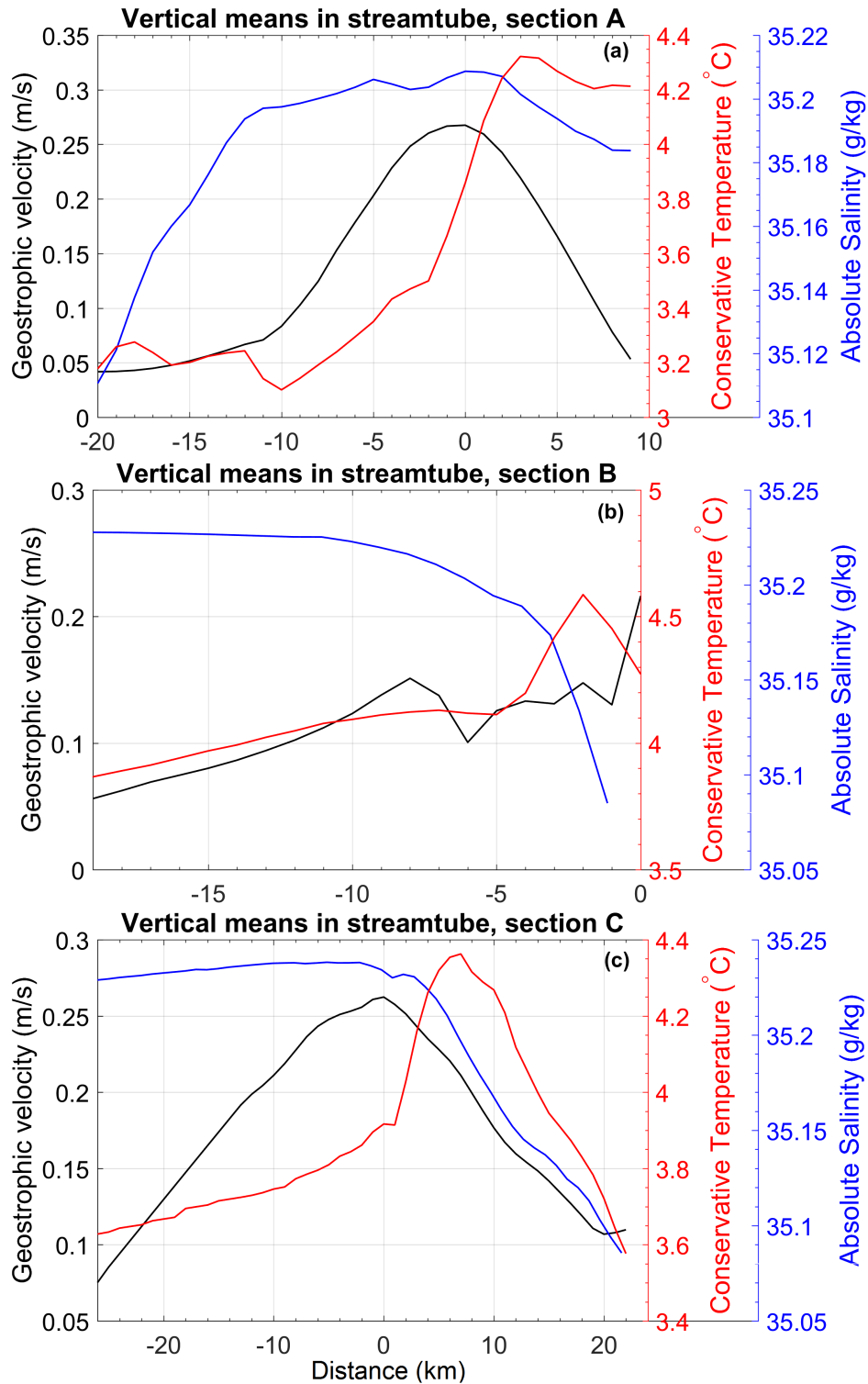
Figure 4.8 – Vertical means of geostrophic velocity, conservative temperature, and absolute salinity, within the main body of streamtube A (a), B (b) and C (c). The distance is set to 0 at the maximum geostrophic velocity.

Table 4.2 – Northward gradients and mean northward heat change. Weighted values are calculated from the weighted mean temperature and salinity (table 4.1), and the arithmetic values are calculated from the arithmetic means.

Mean northward properties	Average	Weighted Average
$d\Theta/dy$ per 100 km (°C)	-0.18 [-0.13, +0.03]	-0.15 [-0.05, +0.02]
dS_A/dy per 100 km $(g\ kg^{-1})$	-0.011 [-0.003, +0.005]	-0.016 [-0.002, +0.001]
$\overline{\text{Heat change}} \times 10^6$ $(W\ m^{-1})$	-13.2 [-13.5, +2.91]	-11.7 [-5.58, +1.64]
Bulk $\overline{F_H}$ $(W\ m^{-2})$	-331 [-188, +47]	-292 [-43, +21]

remains high while the temperature drops. The temperature maximum is found 4 km landward of the geostrophic velocity maximum. The salinity is at about the same location as the geostrophic velocity maximum.

4.3.2   Streamtube B

The streamtube in section B (figure 4.7b), hereby referred to as streamtube B, has a cross section area of 7.7 [+12.4, -2.4] km^2, and a corresponding mean geostrophic velocity, V_{ges}, of 0.10 [-0.04, +0.00]. It is the smallest streamtube, however, it has the largest errors. The current velocities over the Yermak Plateau are weak, and the 0.01 m s^{-1} boundary includes more than 61 km of the 94 km wide section, whereas the 0.07 m s^{-1} boundary includes only 23.7 km. Thus, the volume transport ranges between 0.5 Sv and 1.3 Sv. The volume transport within the 0.04 m s^{-1} boundary is 0.8 Sv, much less than the 3.6 Sv passing through tube C, hence, some of the Atlantic water passing through tube C must recirculate or find a different path into the Arctic Ocean. The mean temperatures (arithmetic and weighted) in streamtube B are the highest mean temperatures amongst all the streamtubes, suggesting that only the warmest, landward part of tube C reaches tube B. The bulk heat flux in streamtube B is -234 W m^{-2} and -206 W m^{-2} for the arithmetic and weighted calculations, respectively. Note, the 0.04 m s^{-1} contour in figure 4.7b continues seaward from where the solid blue line cuts it off, and since it is also Atlantic water seaward, the tube could have been extended seaward. However, as this study will argue for later, the inner branch of WSC is thought to split up where the tube has been cut off, therefore it has not been extended.

Figure 4.8b shows the vertical means within streamtube B. The geostrophic velocity peaks at the landward edge of the tube (0 km), in fact the geostrophic velocity continues

to increase landward outside the tube, but is not captured by the tube because there is no Atlantic water there (see figure 4.3b). The geostrophic velocity is horizontally unsymmetrical, showing multiple local maxima. The vertical mean salinity shows the salinity increasing seaward. The vertical mean temperature is the only property showing a somewhat symmetric shape with colder waters both landward and seaward of the -2 km mark.

4.3.3   Streamtube A

The streamtube in section A (figure 4.7a), hereby referred to as streamtube A, has a cross section area of 8.0 [+3.7, -1.6] km^2, and a corresponding mean geostrophic velocity, V_{ges}, 0.14 [-0.03, +0.03] m s^{-1}. The volume transport is estimated to be 1.1 [+0.2, 0.0] Sv, thus having a larger volume transport than tube B, but within the error estimates. The mean temperatures (arithmetic and weighted) are significantly lower within the tube A than within tubes B and C, requiring a significant cooling of Atlantic water as it moves northward. The bulk heat flux in streamtube A is -266 W m^{-2} -235 W m^{-2}, from the arithmetic and weighted mean calculations, respectively.

Figure 4.8a shows that streamtube A has a symmetric core in velocity, while the temperature maximum is a little landward of the geostrophic velocity maximum. The temperature maximum is at 4 km, decreasing rapidly seaward. The salinity maximum is at 0 km, decreasing slowly at first, then rapidly as the tube reaches into the fresh, cold intrusive layer that can be seen at -12 km in figure 4.1a.

4.3.4   Northward gradients

Figure 4.9 shows the northward change in tube-averaged temperature and salinity. In all tubes, the weighted mean temperature and the weighted salinity are higher than the arithmetic mean, supporting that the weighted means are closer to the core properties of the tubes. The mean temperature in streamtube B is much higher than in tube A and C. A likely explanation for this is that tubes A and C include colder AW that does not flow over the Yermak Plateau, through streamtube B. Relatively broader shelf regions and weaker currents in sections C and A allow the AW to interact with cold shelf waters, reducing the AW temperature. It should be noted that the arithmetic mean temperature within the 0.01 m s^{-1} boundary in section B is 3.72°C, a value that would be lower than the lowest mean temperature in section C, and so, would fit much better into a linearly decreasing temperature. However, the lowest weighted mean temperature in tube B is 3.92°C, still higher than the lowest weighted mean temperature in tube C. Table 4.2 shows the temperature and salinity gradients, and the mean northward heat change from section C to A. The heat change calculated from weighted means is -11.7

[-5.58, +1.64] W m^{-1}, and the corresponding bulk heat flux, $\overline{F_H}$ is -292 [-43, +21] W m^{-2}. Thus, the observed heat change suggest the presence of mechanisms capable of diverging vast amounts of heat as the WSC flows northward.
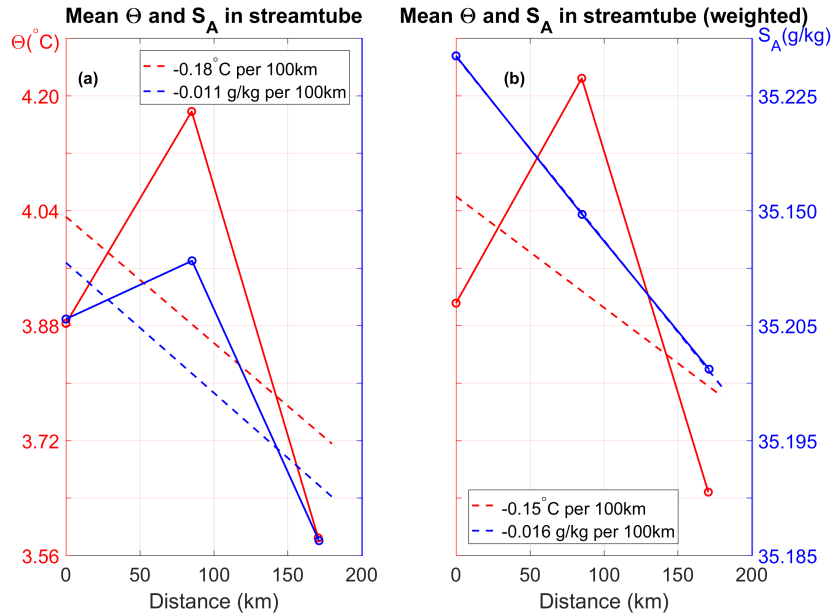

Figure 4.9 – Northward gradients of salinity and temperature, based on arithmetic means within streamtubes (a), and based on averages weighted with geostrophic velocity (b). Dashed lines show the best linear fit with gradients indicated in the legends. Distance is the along path distance from section C to A.

4.4   MIMOC

The Monthly Isopycnal and Mixed-layer Ocean Climatology (MIMOC) described in section 3.1.4 was used for comparing data collected during the cruise to average conditions. MIMOC is representative of modern time (2007-2011) climatological conditions. The comparison is made to assess whether the cruise period was representative of typical conditions in the region.

Upper panels in figure 4.10 show the August data from MIMOC, for Conservative Temperature, Θ, and Absolute Salinity, S_A. Along section C, MIMOC data show that the temperature at 100 dbar pressure exceeds 4.0°C, and salinities are above 35.18 g kg^{-1}. Along section B, temperatures are between 3.0°C and 3.4°C, and salinities are between 35.06 and 35.1 g kg^{-1}. Along section A, temperatures are between 2.2 and 2.6°C, and salinities are between 34.98 g kg^{-1} and 35.02 g kg^{-1}.

Lower panels in figure 4.10 show Θ and S_A measured during the cruise. It is clear that both higher temperatures and higher salinities are found further north than they are in the climatology. Temperatures along section C, B and A exceed 4.8°C, 4.6°C and 4.4°C respectively. That is, temperatures during the cruise were 0.8°C, 1.2°C and 1.8°C higher than the climatology temperatures along section C, B and A, respectively. Salinities along section C, B and A exceed 35.28 g kg^{-1}, 35.24 g kg^{-1} and 35.22 g kg^{-1} respectively, thus being about 0.1 g kg^{-1}, 0.14 g kg^{-1} and 0.2 g kg^{-1} higher than the climatology salinities along section C, B and A, respectively.

Observed fields at 100 dbar show that warm and saline waters are carried northward along the 1000-m isobath. This contradicts the findings in figure 4.6, where currents along the 800-m/900-m/1000-m isobaths north of 79°40′ are directed southward and southwestward. This indicates that the currents measured in this area, at the time of the cruise, are not persistent, and likely often reversed in order to transport AW north along the isobaths as observed.

Figure 4.11 shows Θ and S_A averaged between 100 dbar and 600 dbar for August MIMOC data and cruise data. 100 dbar to 600 dbar is the typical reach of AW. Average values of Θ and S_A show that warmer and saltier waters are found further north during the cruise (fig. 4.11 lower panels) than what is normal according to the climatology (fig. 4.11 upper panels). Mean temperatures along section A are as much as 1.8°C warmer in the cruise data than in the MIMOC data. Mean salinities along section A are as much as 0.12 g kg^{-1} higher during the cruise than in the MIMOC data. Observations show that warm and saline waters are transported northward along the 1000-m isobath.
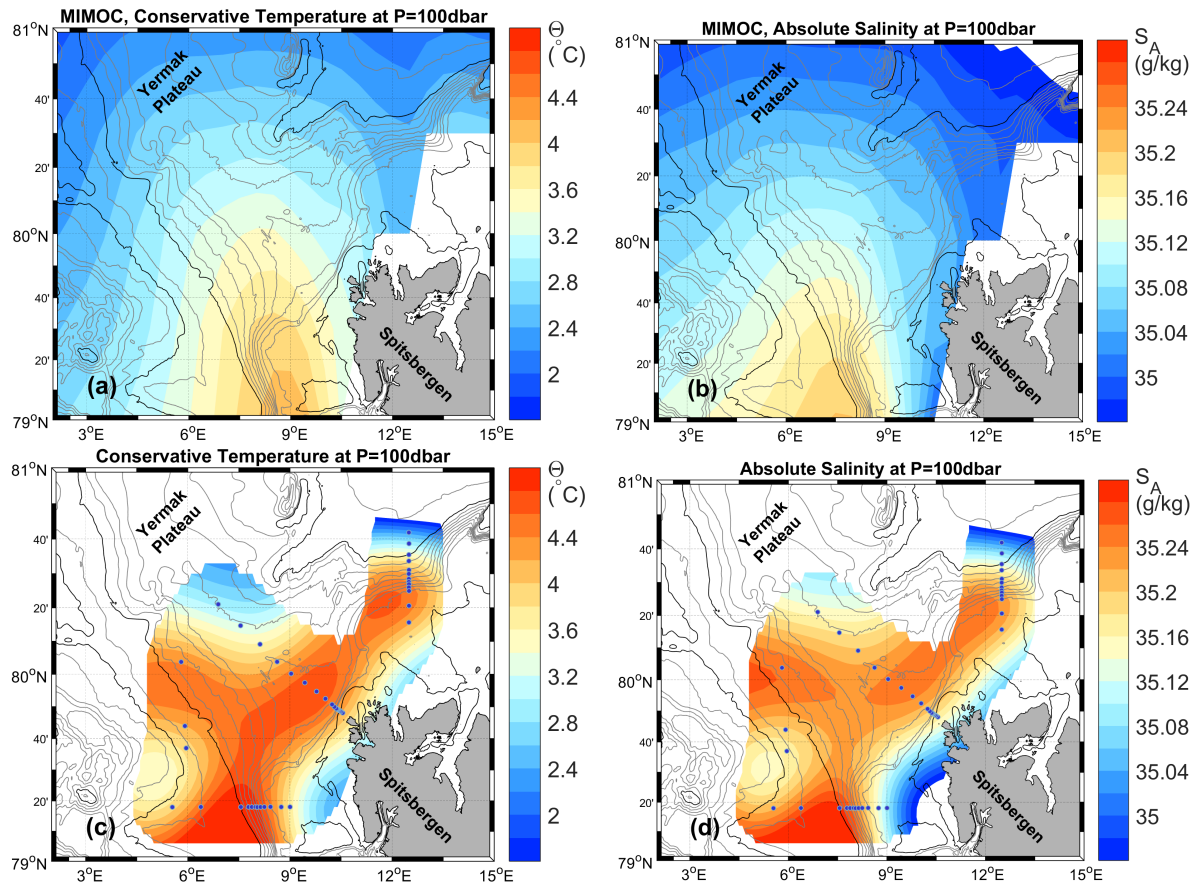
Figure 4.10 – Conservative Temperature and Absolute Salinity data, at 100 dbar pressure level, from (upper panels) the Monthly Isopycnal and Mixed-layer Ocean Climatology and (lower panels) from the cruise. Dots mark the station positions. The cruise data have been objectively analyzed, and data where the error variance exceed 40% of the total variance have been removed.

Figure 4.11 – Same as for figure 4.10, but vertical means between the 100 dbar and 600 dbar levels.

4.5 Microstructure profiles

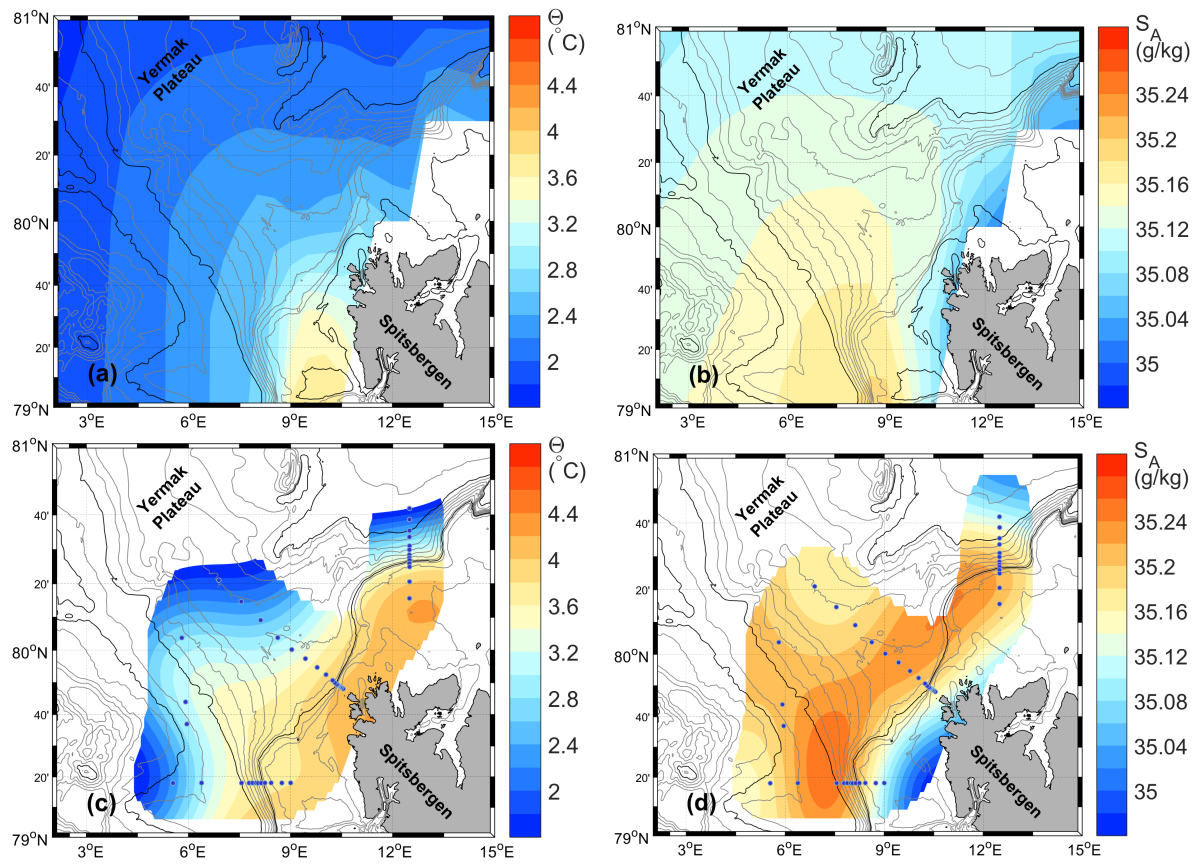For section A, B and C, mean profiles of hydrography, dissipation rate of TKE, diapycnal eddy diffusivity K_ρ and vertical heat flux are shown in the following figures. In general, the temperatures decrease with depth, and turbulent heat fluxes are mostly negative, mixing heat downward. The dissipation rate of TKE is moderate, but mostly below 10^{-8} W kg^{-1}. Next, the microstructure measurements along section A, B and C are described separately. Table 4.3 shows the calculated mean heat flux through the upper and lower boundary of the Atlantic water, and the mean and minimum heat flux within the AW layer. Figure 4.13 shows turbulent heat flux plotted versus potential density for the repeated stations R1 and R4.

4.5.1 Microstructure measurements, Section A

Figure 4.12 shows the temporal mean of 13 VMP casts done at station R1, located between CTD station A7 and A8 (see figure 3.1), on the continental slope. Only at the surface does the dissipation of TKE exceed 10^{-8} W kg^{-1} (c), and the heat flux here is -10 W m^{-2} (e). At the top of the AW (between the upper two dashed lines) the heat flux is -3 W m^{-2} and at the bottom it is -1 W m^{-2} (see table 4.3, R1). The net heat flux is +1 W m^{-2}, hence, the water in the streamtube is warmed from the surface. The heat flux within the boundaries of the AW peaks at 150 m depth, where it is -4 W m^{-2}, potentially due to vertical shear instabilities in the current. Heat flux of similar magnitude as at the surface are found near the seabed, due to intensified dissipation rates in the bottom boundary layer.

The black line in figure 4.13 shows the turbulent heat flux plotted versus density, for station R1. Above the AW layer, heat fluxes indicate two events of shear instabilities, advecting heat downwards in the water column.

Figure 4.14 shows the mean microstructure measurements along section A, for station A9 to A13 in the upper 600 m. In (a), the temperature increases with depth in the upper 15 m. From 15 m through the upper boundary of AW, the temperature decreases. Within the AW layer, the temperature increases to a local maximum at 100 m depth, showing the typical AW temperature maximum. The salinity increases from the surface down to 320 m, and decreases below this, showing the typical AW salinity maximum. The upper boundary of Atlantic water is located between the two upper dashed gray lines, and the lower boundary of the AW is located between the two lower dashed gray lines. The dissipation of TKE is near 10^{-8} W kg^{-1} at the surface(c), decreasing with depth until it becomes smaller than the noise level (10^{-10} W kg^{-1}) at 520 m depth. Diapycnal eddy diffusivity and turbulent heat fluxes are small within the AW layer.

Table 4.3 – Turbulent heat fluxes from microstructure measurements between the upper and lower boundaries of the Atlantic water (AW). Values are rounded to the nearest integer.

Turbulent heat flux ($\mathrm{W\ m^{-2}}$)	R1	R2	R3	R4	A	C
Across AW upper boundary	-3	-1	-1	-2	-2	-1
Across AW lower boundary	-1				0	0
Average within AW	-1	-1	-8	-1	0	0
Minimum within AW	-4	-12	-39	-12	-4	-2
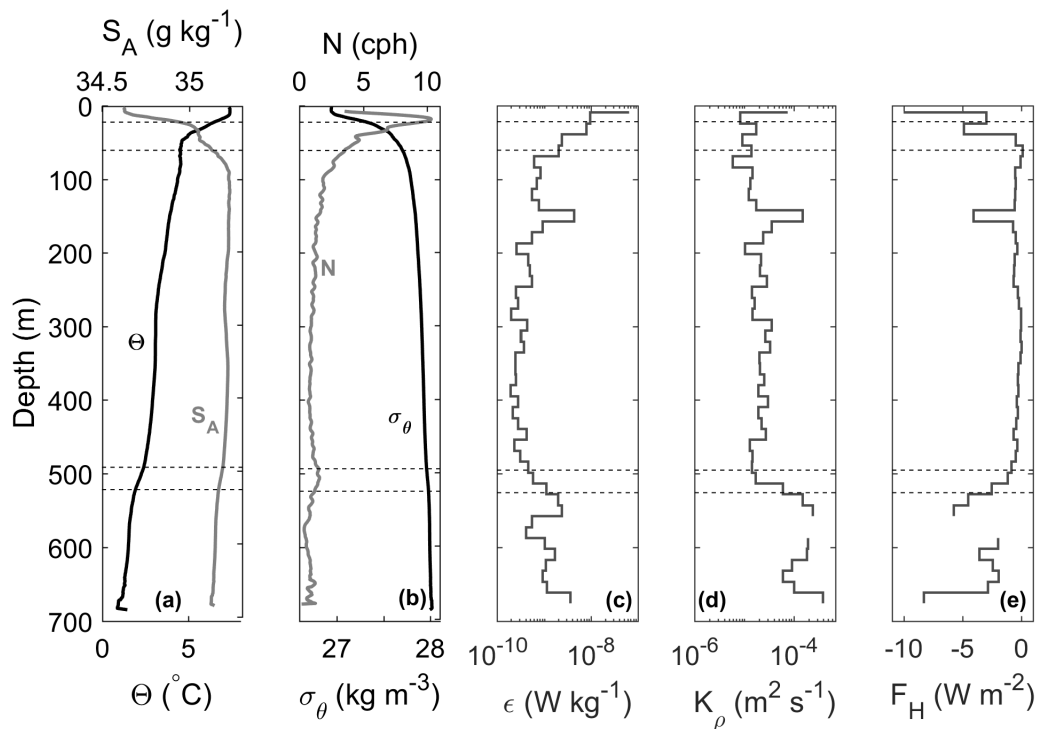
Figure 4.12 – Temporal mean of microstructure measurements at station R1, section A. (a) Temperature Θ (black) and salinity S_A (gray), (b) potential density anomaly σ_θ (black) and buoyancy frequency N (gray), (c) 15-m bin-averaged dissipation of TKE ϵ, (d) eddy diffusivity K_ρ (eq. 3.23), and (e) vertical heat flux F_H. $N^2 < 1 \times 10^{-6}$ was removed before calculating K_ρ and F_H. The dashed lines envelop the upper and lower boundaries of the streamtube, similar to the density lines in figure 4.7a.

Figure 4.13 – Heat flux plotted against potential density. The two dashed lines show typical upper and lower boundary of AW in density. Heat fluxes are averaged in 0.05 kg m^{-3} density change bins.
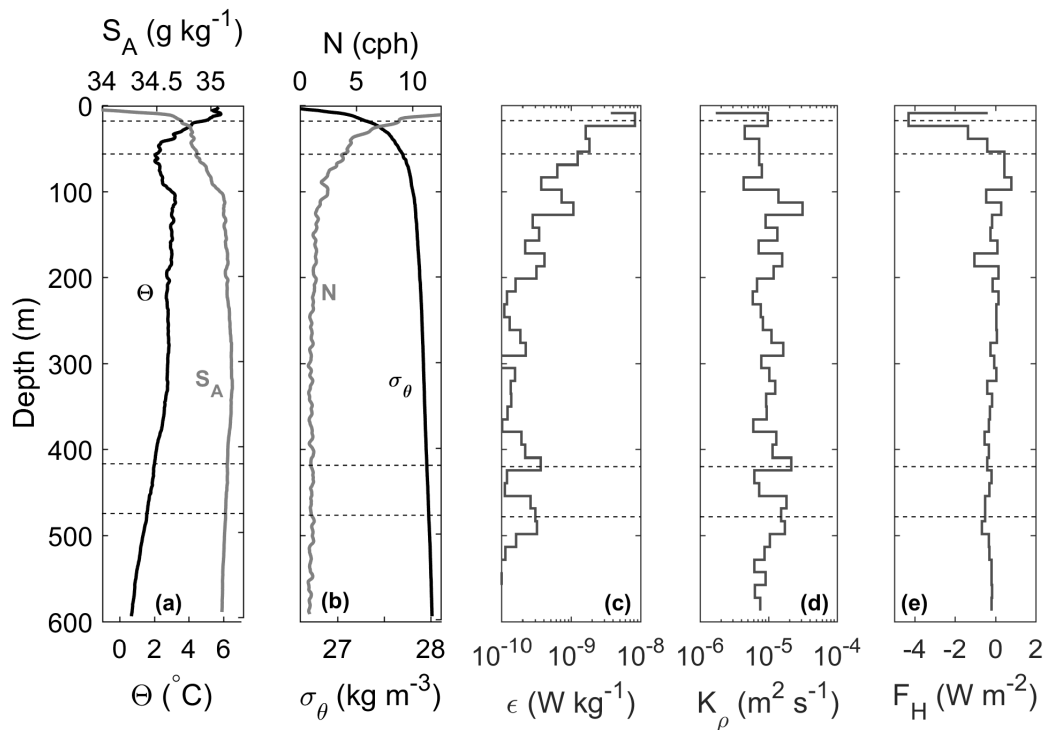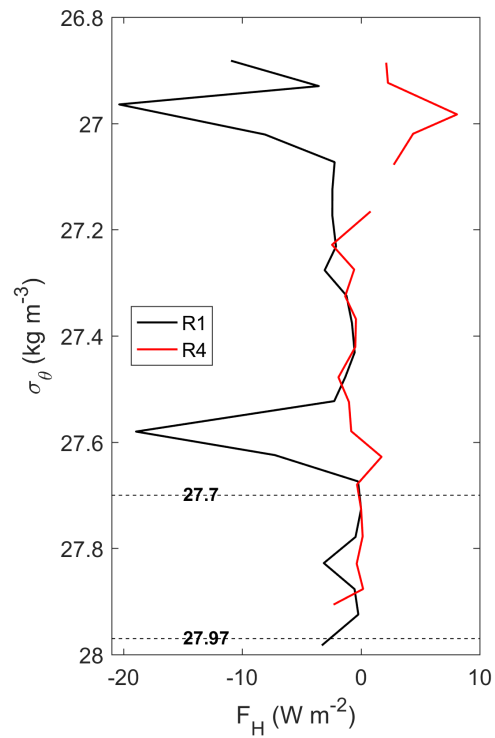

Figure 4.14 – Horizontal mean along section A, away from the continental slope and the bottom boundary layer. The horizontal mean is calculated for station A9 to A13, in the upper 600 m. Otherwise, the figure shows the same as figure 4.12.

The mean heat flux within, and out of the bottom boundary of the AW is nil W m^{-2} (see table 4.3, A), resulting in a net heating from the surface.

4.5.2   Microstructure measurements, Section B

Along section microstructure measurements were not collected along section B. Instead, VMP measurements were collected at two repeated stations, R2, and R3. R2 was located near CTD station B15 (see figure 3.1), while R3 was located near CTD station B6. Figure 4.15 shows the temporal mean of 13 VMP casts at repeated station R2. The dissipation of TKE is small everywhere (c). Only at the surface is it larger than 10^{-8} W kg^{-1}. The heat flux is close to zero everywhere except near the seabed where it is -12 W m^{-2} (e), and the eddy diffusivity is 4×10^{-4} m^2 s^{-1} (d). The temporal mean of 13 VMP casts at repeated station R3 is shown in figure 4.16. At the repeated station R3 the dissipation rate of TKE is mostly greater than 10^{-8} W kg^{-1} (c), much higher than the dissipation rate at station R2. At the surface and near the seabed the dissipation rates are similar, and relatively high, with values close to 2×10^{-7} W kg^{-1}. The diapycnal eddy diffusivity is mostly above 10^{-4} m^2 s^{-1}, exceeding 10^{-3} m^2 s^{-1} at 150 m depth and just below 200 m depth (d). The heat fluxes at station R3 are large (e). At the surface, the heat flux is -89 W m^{-2}, and within the Atlantic water, the largest heat flux is at 140 m depth, where it is -39 W m^{-2}.

4.5.3   Microstructure measurements, Section C

Figure 4.17 shows the temporal mean of 15 VMP casts at the repeated station R4. Station R4 is located between CTD stations C7 and C8 (see figure 3.1). Dissipation of TKE exceeds 10^{-8} W kg^{-1} only at the surface and at the bottom (c). The eddy diffusivity is large in the bottom boundary layer (d), with values around 10^{-3} m^2 s^{-1}. The temperature gradient near the bottom is small (a), and the heat fluxes are no larger than -12 W m^{-2} (e) even though the eddy diffusivity is relatively large. Elsewhere within the AW layer, the heat flux is close to zero, and the dissipation of TKE is near the instrument noise level (10^{-10} W kg^{-1}).

The red line in figure 4.13 shows the turbulent heat flux plotted versus density, for station R4. Heat fluxes are small everywhere except at the surface where it indicates heat loss to the surface.

Figure 4.18 shows the horizontal mean microstructure measurements along section C, away from the continental slope and bottom boundary layer. At the surface (upper 15 m), the temperature increases with depth (a), the dissipation of TKE is close to 10^{-7} W kg^{-1} (c), and the heat flux is +10 W m^{-2} (e). Elsewhere the temperature decreases with depth. The eddy diffusivity below the surface boundary layer is close
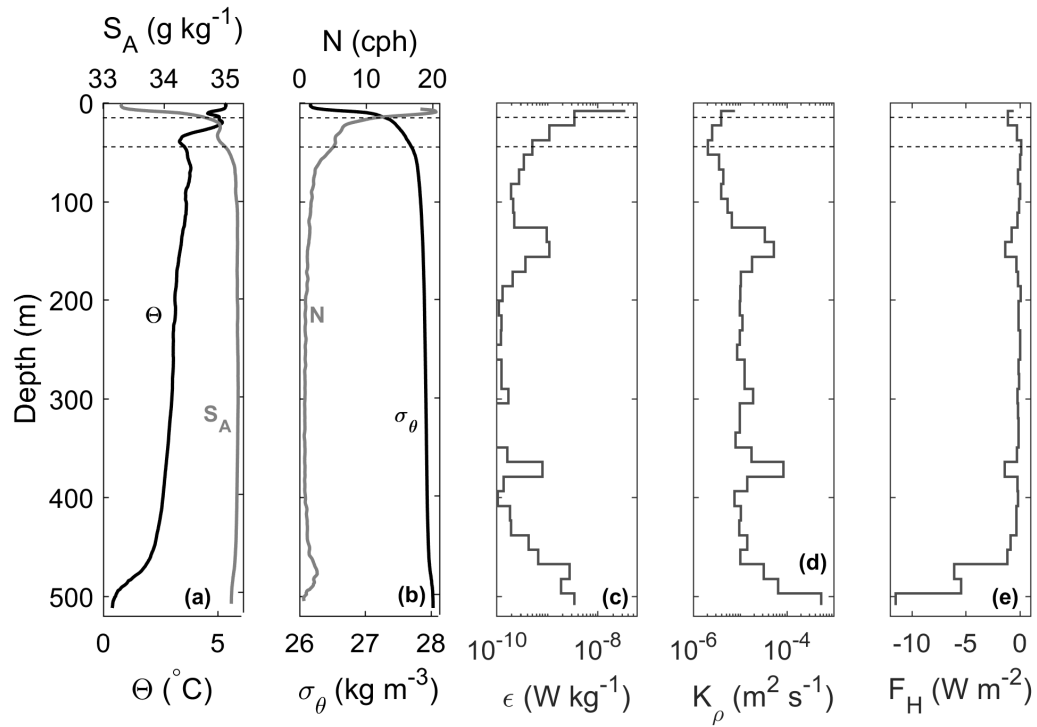
Figure 4.15 – Same as figure 4.12, but for station R2, section B.
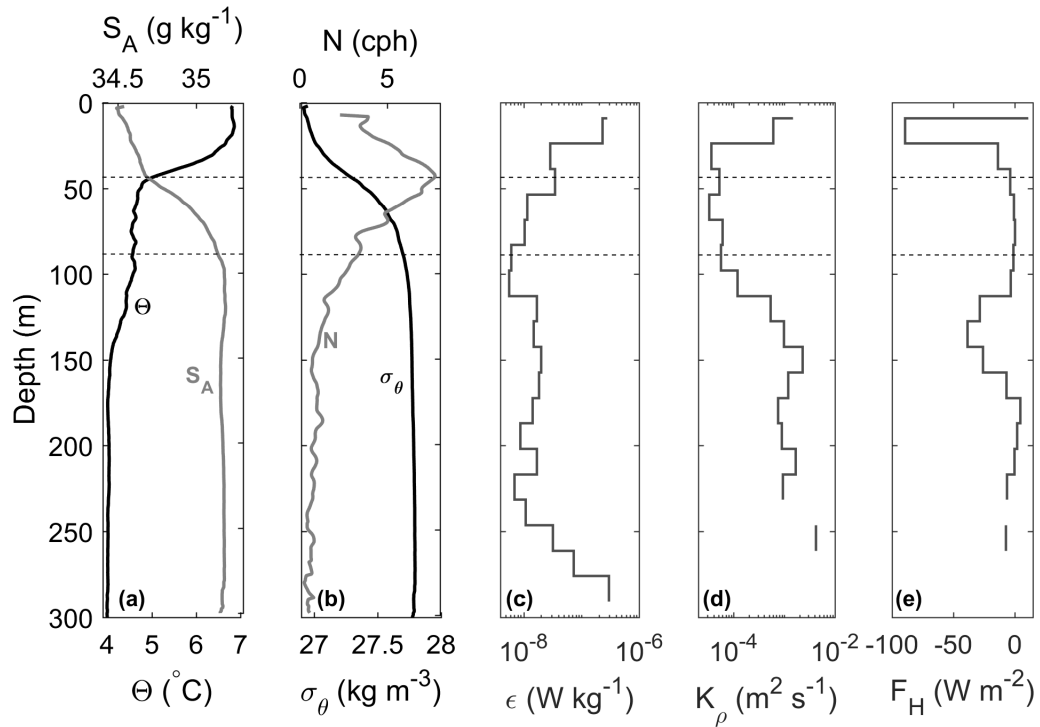
Figure 4.16 – Same as figure 4.12, but for station R3, section B.
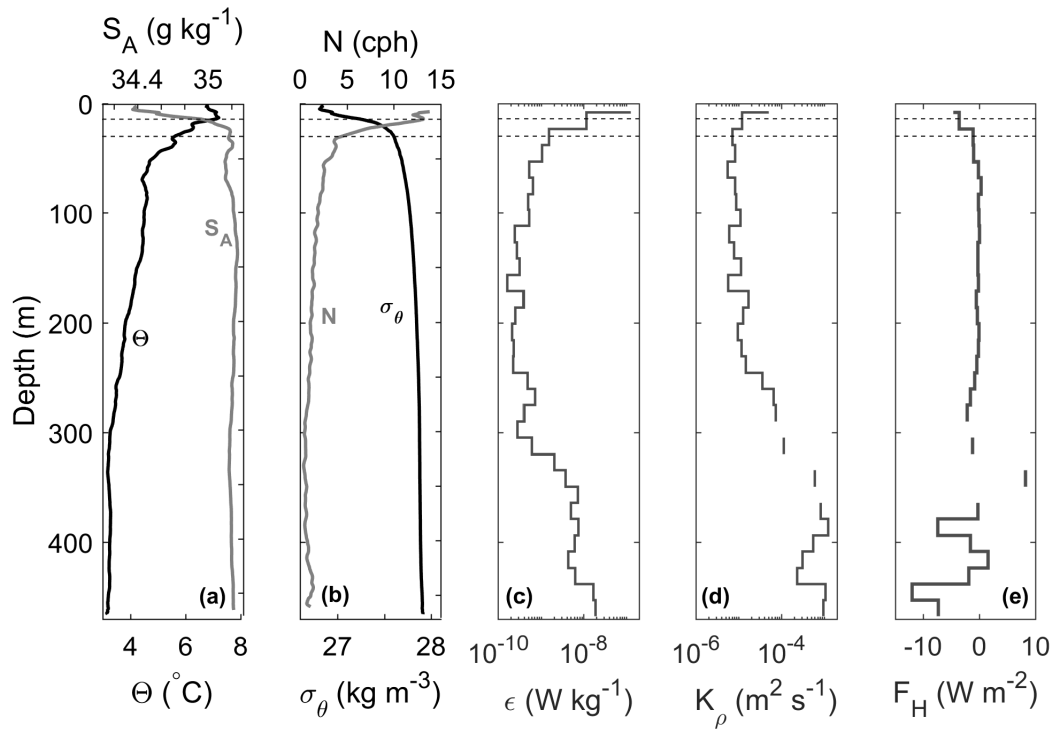
Figure 4.17 – Same as figure 4.12, but for station R4, section C.
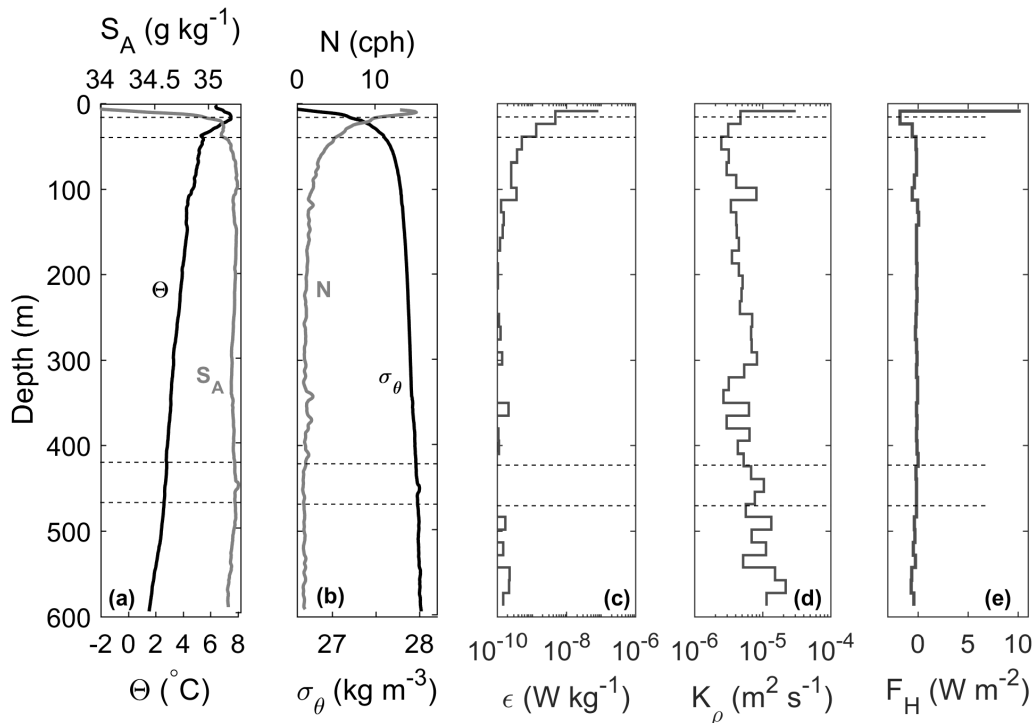
Figure 4.18 – Horizontal mean along section C, away from the continental slope and the bottom boundary layer. The horizontal mean is calculated for station C1 to C5, in the upper 600 m. Otherwise, the figure shows the same as figure 4.12.

to the instrument noise level. The mean heat flux within the AW layer and through the lower boundary of AW is nil W m^{-2} (see table 4.3). The mean turbulent heat flux through the upper AW boundary is -1 W m^{-2}, resulting in a net AW heating.

5 | Discussion

5.1 Hydrography and Water masses

The August hydrographic conditions presented in this study show surface temperatures as high as 8°C, and temperatures decreasing with depth in all three sections (figure 4.1). Only the northern part of section A shows cold surface waters. These are summer conditions, and not the typical Arctic Ocean temperature profile where a temperature maximum is usually found below 50 m depth, marking the core of Atlantic water. August is normally the time of year when the upper ocean is at its warmest, however, comparing observations in this study with other studies suggest that the August 2015 conditions were particularly warm, not only near the surface. October/November 2001 observations west of Svalbard, reported by Cokelet et al. (2008), show that AW temperatures above 4°C are separated from the surface by colder water, similar to winter (January/February) observations by Boyd and D'Asaro (1994) in 1989. Also September 2012 observations north of Svalbard (81°30′N, 30°E), show AW temperatures near 4°C separated from the surface by colder water (Våge et al., 2016). Upper left panel compared to lower left panel in figure 4.10 and 4.11 clearly show that August cruise conditions were as much as 1.8°C warmer than the August climatology data. 2015 spring observations from drifts north of Svalbard support the findings of AW being warmer and shallower than the climatology (Meyer et al., 2016).

The salinity maximum is found beneath the surface in all three sections, between 100 m and 400 m depth. This is consistent with previous studies in this region (Cokelet et al., 2008; Våge et al., 2016; Meyer et al., 2016). Compared to the climatology, the cruise data show higher salinities along all sections (see figure 4.10b, 4.10d, 4.11b and 4.11d).

The $\Theta - S_A$ diagrams in figure 4.4 show that the formation of LAIW, UAIW and DW is dominated by atmospheric cooling, that is, the heat loss to atmosphere vs heat loss to sea ice ratio (Q/H) is more than 5/1. In the formation of PIW, heat loss to sea ice and atmosphere is equally important $(Q/H = 1)$. The above is consistent with previous observations by Boyd and D'Asaro (1994) and Cokelet et al. (2008).

The formation of ASW does not follow a clear Gade line in the $\Theta - S_A$ diagrams, which is different from the October/November observation by Cokelet et al. (2008) and January/February observations by Boyd and D'Asaro (1994). In section C, ASW follows Gade lines corresponding to $Q/H = 0$, that is, ASW comes from AW melting sea ice, but in section B and A, the ASW formation does not follow any of the illustrated Gade lines. This is most likely because warm and relatively fresh surface water (from earlier melting events) has mixed with AW near the surface, and the transformation process cannot be represented by the Q/H lines.

The objective analysis of temperature and salinity in figure 4.10c and 4.10d, respectively, shows that AW properties are carried along the 1000-m isobath northward. The same signal is seen in figure 4.11c and 4.11d, showing the objective analysis of the AW depth average. However, from the depth average, it is clear that the AW loses its temperature signal much faster than its salinity signal, suggesting mixing with colder, salty water, such as LAIW. In figure 4.3, showing the water masses found in the different sections, it is clear that LAIW is found higher in the water column seaward, potentially due to heat loss along isopycnals. This will be discussed further in section 5.4.

5.2   Currents and Circulation

Currents along sections A, B and C have a strong barotropic component (figure 4.5), driven by geostrophic balance. The geostrophic currents along section A and inner part of section C (fig. 4.5a and 4.5g) are symmetric with respect to cross-section distance, whereas the geostrophic current along section B (fig. 4.5d) is not. This is also visible in figure 4.8, where the black lines show the vertical mean of the geostrophic velocity within the different streamtubes. The symmetry depends on the slope where the current is located. In sections A and C, the currents are located over relatively even slopes continuing into deep waters, whereas in section B the slope is not even, and it abruptly ends on the shallow Yermak Plateau, causing the current to spread out over the Yermak Plateau.

The objective analysis of the upper 500m average currents from VMADCP data, show a well-defined Svalbard branch of the WSC along the 400-m isobath (figure 4.6). The Yermak branch however, is not well defined. In fact, currents along the 1000-m isobath are opposite of what might be expected. Instead, there is a recirculation carrying AW westward and northward along the outer edge of the Molly Hole (cf. figure 2.1). North of the MH, the currents are westward, consistent with earlier finding by Hattermann et al. (2016), who state that the main recirculation route for the warmest AW is north of the MH. However, AW temperature and salinity properties are found along the 1000-m isobath (see figure 4.10 and 4.11), supporting a Yermak Branch. It is

likely that the cruise survey was affected by a synoptic event causing a Yermak branch reversal.

On the seaward side of section B (-75 km), there is a barotropic current flowing southwest (4.5d, e, and f) consisting of AW (fig. 4.3b), for now referred to as the "negative branch". On the landward side, the current flowing northwest is nearly separated in two different branches at -25 km. If the two northwestward flowing branches diverge, a possible path for the outer branch, for now referred to as the "positive branch", is to recirculate as the negative branch. The following calculations only include Atlantic Water in the positive and negative branch.

The mean geostrophic velocity of the positive branch is 0.03 m s^{-1}, while it is -0.04 m s^{-1} in the negative branch. The associated volume transport is 0.44 Sv and -0.41 Sv, for the positive and negative branch respectively. Hence, the positive and negative branch volume transport balance within measurement uncertainties, making a recirculation plausible. However, the mean temperature and mean salinity in the positive branch is 3.41°C and 35.205 g kg^{-1}, while it is 2.75°C and 35.196 g kg^{-1} in the negative branch. Thus, if the positive branch recirculates as the negative branch, it loses a significant amount of heat and salt in its path. The currents in the positive and negative branch are both weak, and since the ADCP error is ±0.03 m s^{-1}, the error estimates in these calculations would be relatively large. The objective analysis of the upper 500 m vertical mean of VMADCP currents (figure 4.6) does support a potential recirculation along section B. However, the currents are weak, and based on the limited observations along section B, a conclusion to whether there is an ongoing recirculation or not, cannot be drawn.

5.3   Streamtubes

Vertical averaged properties in figure 4.8 show that streamtubes C and A are horizontally symmetric in geostrophic velocity, with the temperature maximum located landward and the salinity maximum approximately co-located with the geostrophic velocity maximum. The symmetric geostrophic current breaks down over the YP in streamtube B, where the steep continental slope abruptly ends on the shallow YP. This lack of symmetry along section B makes it difficult to define the boundaries of streamtube B, and it follows that streamtube B calculations have large error estimates.

5.3.1 Volume transport

Streamtube C

The volume transport in streamtube C (see figure 4.7c) is estimated to be 3.6 [+0.1, -0.2] Sv. Beszczynska-Möller et al. (2012) estimated that the long-term mean net volume transport of Atlantic Water between 1997 and 2010, along the array of moorings at 78°50′N, was 3.0±0.2 Sv. The August mean transport in the same period was 2.5±0.7 Sv, and individual August means were observed to be as high as 3.6 Sv (Beszczynska-Möller et al., 2012). The volume transport estimated by Beszczynska-Möller et al. (2012) is for AW roughly between the 2600-m isobath and the 300-m isobath. In contrast, streamtube C is located between the 1500-m isobath and the 140-m isobath. Hence, the volume transport estimated through streamtube C, in this study, is larger than both the annual mean and the August mean estimated by Beszczynska-Möller et al. (2012), even though streamtube C covers a smaller area than the estimate by Beszczynska-Möller et al. (2012). However, section C in this study is only a synoptic picture, and day-to-day or week-to-week variations are unknown.

Streamtube B

The volume transport in streamtube B (see figure 4.7b) is estimated to be 0.8 [+0.5, -0.3] Sv, and the mean temperature within the streamtube is 4.18 [-0.46, +0.22]°C. The large error is due to relatively slow currents through most of section B, making the boundaries of the tube very uncertain.

If the inner branch of the WSC strictly follows the f/h contours, it should be possible to estimate how much of the volume in streamtube C flows over the Yermak Plateau, through streamtube B. The outer edge of streamtube B is located over the 475-m isobath. Streamtube C is 0.5° south of streamtube B, and h in tube C is 475.8 m, not significantly different than 475 m. Calculating the volume transport landward of the 475-m isobath in streamtube C, gives 0.6 Sv, which is within the uncertainty of tube B volume transport. The mean temperature of AW landward of the 475-m isobath in tube C is 4.05°C, still lower than the mean temperature in tube B, but well within the uncertainty.

Streamtube A

The volume transport in streamtube A (see figure 4.7a) is estimated to be 1.1 [+0.2, 0.0]. During a scientific cruise north of Svalbard in September 2012, Våge et al. (2016) estimated an AW volume transport of 1.6 ± 0.3 Sv. Although the latter is a higher estimate than this study, the error estimates overlap. The estimate by Våge et al.

(2016) was 340 km downstream of streamtube A, at 81°50′N and 30°E, and instead of using salinity to define AW, they used density criteria. Following Rudels et al. (2005), Våge et al. (2016) considered AW to be within the density range $27.70 \leq \sigma_\theta \leq 27.97$ kg m^{-3} and warmer than 2°C. As seen in figure 4.7a, these density lines fit streamtube A well. Våge et al. (2016) also included all AW with geostrophic velocity higher than 0 m s^{-1}, whereas in streamtube A, the boundary is drawn at 0.04 m s^{-1}, which can account for some of the discrepancy. The main difference between the geostrophic estimate in streamtube A and the geostrophic estimate by Våge et al. (2016) is that in tube A, the barotropic currents are bound landward of the 800-m isobath, whereas Våge et al. (2016) found barotropic currents 20 km seaward of the 800-m isobath.

For comparison with volume transport in streamtubes B and C, the volume transport landward of the 475-m isobath in streamtube A is estimated to be 0.4 Sv. This is lower than the estimates in streamtube B and C. To get 0.6 Sv, comparable to landward of the 475-m isobath in streamtubes B and C, we have to include volume transport landward of the 575-m isobath in streamtube A. Whether an event has caused the current to shift seaward, or whether the divergence in current along the continental shelf break (fig. 4.5-Section A) has caused a decrease in volume transport is unclear. The lack of a well-defined slope on the shelf in Section B may lead to the break of topographic control and meander the current to deeper isobaths.

If between 0.6 Sv and 0.8 Sv flows through streamtube B towards streamtube A, it follows that between 0.3 and 0.5 Sv is transported by the Yermak branch in order for volume to be conserved.

The barotropic currents in streamtube A are bound landward of the 800-m isobath. Calculating the volume transport landward of the 800-m isobath in streamtube C, gives 1.4 Sv. This is higher than the volume transport in streamtube A, however, loosing AW to the formation of LAIW and ASW, and to eddy recirculation, can be expected.

5.3.2   Cooling of WSC

Estimated bulk heat flux

The arithmetic mean northward temperature gradient is estimated to be -0.18 [-0.13, +0.03]°C per 100 km, and the weighted mean is -0.15 [-0.05, +0.02]°C per 100 km (see table 4.2). Previous research on the temperature gradient along the WSC during summer/fall has yielded the following results. Cokelet et al. (2008) observed -0.19°C/100 km during October and November 2001. Saloranta and Haugan (2004) observed a 50 year summer mean cooling of -0.20°C/100 km. Helland-Hansen and Nansen (1912) found a -0.20°C/100 km cooling in 1910, between 75°N and 79°N. The temperature gradients found in this study are not significantly different from previous findings.

The heat changes corresponding to the observed northward temperature gradients are estimated to be -331 [-188, +47] W m^{-2} and -292 [-43, +21] W m^{-2}, for the arithmetic and weighted temperature gradient respectively. It is clear that the arithmetic means yield large error estimates, and are very sensitive to where the boundaries of the streamtubes are drawn. As such, the average values weighted with geostrophic velocities are likely closer to the true properties of the WSC.

The estimated bulk heat fluxes are comparable to the 50 year mean summer heat flux of -330 W m^{-2}, estimated by Saloranta and Haugan (2004) (see section 2.2 for more details). It is also comparable to the 310 W m^{-2} estimated by Cokelet et al. (2008). Boyd and D'Asaro (1994) stated that a heat loss of -20×10^6 W m^{-1} (within a factor of two) was needed to cool the warm core as much as observed. This is comparable to the -26.2 [-21.2, +5.00] $\times 10^6$ W m^{-1} heat loss found in streamtube C. Cokelet et al. (2008) and Saloranta and Haugan (2004) used a mean velocity of 0.1 m s^{-1} when estimating the heat flux. In this study, the mean velocity in each streamtube has been used to calculate an individual heat flux in each tube. The velocities used are 0.14, 0.1 and 0.17 m s^{-1} for tube A, B and C, respectively. From equation 3.19, it is clear that the estimated heat flux is very sensitive to the velocity input. The heat flux increases proportionally with velocity.

Measured turbulent heat flux

The mean turbulent heat fluxes within the AW layer, measured by the microstructure profiler, are found to be between -1 and -8 W m^{-2}, where the largest mean heat flux is found at station R3, within streamtube B over the Yermak Plateau (see table 4.3). Horizontal means away from the continental slope and bottom boundary layer show fluxes close to 0 W m^{-2} within the AW layer. The largest heat flux within the AW layer is -39 W m^{-2}, found at station R3. The small fluxes north and south of the YP are consistent with previous findings in the Arctic region (Sirevaag and Fer, 2009; Krishfield and Perovich, 2005). Elevated fluxes over the YP are consistent with previous finding by Padman and Dillon (1991).

During the period of the cruise reported here, the temperatures decreased with depth, hence all heat fluxes are negative. In section A and C, where AW is above colder LAIW, the heat flux is larger through the top of the AW layer than through the bottom, resulting in net heating. The measured heating of AW from section A and C is -2 and -1 W m^{-2}, respectively. In section B, the AW layer goes all the way to the seabed, and the negative heat flux at the top of the layer contributes to warming the AW.

5.3.3   Divergence of salt

The arithmetic mean northward salinity gradient is found to be -0.011 [-0.003, +0.005] g kg^{-1} per 100 km, and the weighted mean is -0.016 [-0.002, +0.001] g kg^{-1} per 100 km. Cokelet et al. (2008) found a downstream freshening of 0.013/100 km, and Saloranta and Haugan (2004) found a 50 year mean summer freshening of 0.010/100 km, measured in practical salinity scale. The arithmetic mean gradient found in this study is not significantly different from previous findings. The weighted mean gradient on the other hand, is larger than the arithmetic mean, which is surprising considering the weighted mean should be closer to core properties of AW. However, the weighting is done using the geostrophic velocity, which is higher near the surface, near ASW, which is fresher than AW. Hence, the AW salinity core is lower in the water column than the temperature and geostrophic velocity core, and weighting using the geostrophic velocity does not capture the salinity core properly. The salinity plots in figure 4.1 confirms that the salinity maximum of the AW is below the temperature maximum, which is consistent with previous findings.

5.4   Lateral mixing

If the AW is not cooled by vertical mixing, lateral mixing, shelf-basin exchange, and intrusions of cold shelf water must be responsible for the cooling. Dividing the along current heat loss estimate by the thickness of the AW layer (about 400 m) yields the flux through the side of the streamtubes. For streamtube A, B and C, these fluxes are 1.9×10^4 W m^{-2}, 1.4×10^4 W m^{-2}, and 6.5×10^4 W m^{-2}, respectively.

Perkin and Lewis (1984) observed a series of eddies generated where the branches of the WSC split. These eddies play a major role in the salt and heat budget of the Arctic Ocean (von Appen et al., 2016; Hattermann et al., 2016), in addition, properties are diffused along mean isopycnals in a mesoscale eddy field (Haidvogel and Keffer, 1984). The isopycnal eddy diffusivity, K_I can be estimated by $K_I = u'l'$, where u' is the eddy velocity and l' is the eddy length scale (Böning, 1988). Next, the heat flux can be estimated using equation 3.20, but substituting w' with u' and dT/dz with dT/dx.

From the Conservative Temperature panels in figure 4.1, it is clear that AW cools along the isopycnals seaward. The mean horizontal temperature gradient of AW in section A is 0.06°C per km, while for section B and C it is about 0.02°C per km.

In section A, a pattern resembling an eddy is present, with a length scale of about 10 km. The eddy velocity is weak, no more than a few cm/s. Setting u' equal to 0.02 m s^{-1} yields $K_I = 200$ m^2 s^{-1}, which is a reasonable order of magnitude estimate. Multiplying K_I with the horizontal temperature gradient of each section, the density

of sea water, and the specific heat capacity of sea water gives the horizontal heat flux in W m^{-2}. For section A, B and C these are 5.3×10^4 W m^{-2}, 1.7×10^4 W m^{-2} and 1.9×10^4 W m^{-2}, respectively. These heat fluxes are in the same order of magnitude as the needed heat flux if AW was cooled by lateral mixing alone. Hence, all the cooling can be achieved through isopycnal diffusion in an eddy field where the isopycnals are close to horizontal.

At the time of the cruise, AW had warmer and fresher ASW and SSW above, and colder LAIW below. All vertical fluxes were negative, hence vertical cooling was possible only at the bottom of the AW layer. If the vertical mixing was and efficient cooling mechanism, we would expect LAIW to be elevated on the continental slope where the vertical mixing is greater. From the water mass figure 4.3 this is not the case. Instead, the LAIW is higher in the water column seaward. This can be achieved by cooling AW along isopycnals, thus generating LAIW seawards. However, it does require the seaward water to be of roughly the same salinity as AW, or else the transformation would not follow the Gade lines suggesting mostly atmospheric cooling, that is, Gade lines where $Q/H > 5$ (see figure 4.4). From the $\Theta - S_A$ diagram in figure 4.4, it is clear that mixing between cold UAIW and AW will generate LAIW or even DW, and the mixing lines would be equal to the Gade lines where $Q/H > 5$.

6 | Conclusions

The 10 days scientific cruise to the Yermak Plateau, conducted in August 2015, provides a snapshot of the West Spitsbergen Current (WSC) conditions regarding hydrography, transport and mixing, in conditions of no sea ice. Atlantic water is found to be both warmer and saltier north of Svalbard, compared to the MIMOC climatology, supporting the findings of Meyer et al. (2016).

The Svalbard branch of the WSC, follows the 400-m isobath closely. At the time of the cruise, current measurements did not show the Yermak branch following the 1000-m isobath north along the Yermak Plateau. Instead the Yermak branch joined the recirculation around the Molly Hole gyre, as described by Hattermann et al. (2016). However, observed Atlantic water temperature and salinity properties are along the 1000-m isobath, suggest the presence of the Yermak branch, and that our current observations were affected by a synoptic event.

West Spitsbergen Current volume transport south of the Yermak Plateau at 79°20′ is estimated to be 3.6 (3.4, 3.7) Sv, which is higher than both the annual mean and August mean estimated by Beszczynska-Möller et al. (2012) in the period 1997-2010. North of Svalbard, the volume transport is estimated to be 1.1 (1.1, 1.3) Sv, similar to the findings of Våge et al. (2016). North and south of the Yermak Plateau the WSC is horizontally symmetric in velocity, whereas on the Yermak Plateau the symmetry breaks down. The volume transport over the Yermak Plateau is estimated to be 0.8 (0.5, 1.3) Sv, where the high error estimates are due to the lack of symmetry and weak currents. Further research is needed to determine the fraction of Atlantic water transport over the Yermak Plateau, and how much flows around.

Despite a high volume transport south of the Yermak Plateau, and higher AW temperature and salinity than in the climatology, the northward temperature and salinity gradients are similar to previous research. The observed temperature and salinity gradients were -0.15 (-0.20, -0.13)°C and -0.016 (-0.018, -0.015) g kg^{-1} per 100 km. The associated bulk heat flux is estimated to be -292 (-335, -271) W m^{-2}, comparable to findings by Cokelet et al. (2008) and Saloranta and Haugan (2004).

During the period of the cruise, microstructure measurements show that the Atlantic water layer is heated from the surface, and cooled by lower Arctic intermediate water

below, resulting in a net heating. This study finds that lateral mixing seaward, along isopycnals, by eddies is likely the only mechanism capable of cooling AW as much as observed. The fact that lower Arctic intermediate water is found higher up in the water column seaward suggest that AW becomes lower Arctic intermediate water seawards, supporting lateral mixing.

7 | Bibliography

Aagaard, K., Coachman, L. K., and Carmack, E. (1981). On the halocline of the Arctic Ocean. *Deep Sea Research Part A, Oceanographic Research Papers*, 28(6):529–545.

Aagaard, K., Foldvik, A., and Hillman, S. R. (1987). The West Spitsbergen Current: Disposition and water mass transformation. *Journal of Geophysical Research: Oceans*, 92(C4):3778–3784.

Aagaard, K., Swift, J. H., and Carmack, E. C. (1985). Thermohaline circulation in the Arctic Mediterranean Seas. *Journal of Geophysical Research*, 90(C3):4833.

Beszczynska-Möller, A., Fahrbach, E., Schauer, U., and Hansen, E. (2012). Variability in Atlantic water temperature and transport at the entrance to the Arctic Ocean, 1997–2010. *ICES Journal of Marine Science*, 69(5):852–863.

Böning, C. W. (1988). Characteristics of particle dispersion in the North Atlantic: an alternative interpretation of SOFAR float results. *Deep Sea Research Part A. Oceanographic Research Papers*, 35(8):1379–1385.

Boyd, T. J. and D'Asaro, E. A. (1994). Cooling of the West Spitsbergen Current: Wintertime Observations West of Svalbard. *Journal of Geophysical Research: Oceans*, 99(C11):22597–22618.

Carmack, E., Polyakov, I., Padman, L., Fer, I., Hunke, E., Hutchings, J., Jackson, J., Kelley, D., Kwok, R., Layton, C., Melling, H., Perovich, D., Persson, O., Ruddick, B., Timmermans, M.-L., Toole, J., Ross, T., Vavrus, S., and Winsor, P. (2015). Toward Quantifying the Increasing Role of Oceanic Heat in Sea Ice Loss in the New Arctic. *Bulletin of the American Meteorological Society*, 96(12):2079–2105.

Cokelet, E. D., Tervalon, N., and Bellingham, J. G. (2008). Hydrography of the West Spitsbergen Current, Svalbard Branch: Autumn 2001. *Journal of Geophysical Research: Oceans*, 113(1):C01006.

Cushman-Roisin, B. and Beckers, J. M. (2011). *Introduction to Geophysical Fluid Dynamics: Physical and Numerical Aspects*, volume 54 of *International Geophysics*. Elsevier Science, 2 edition.

Cutnell, J. D. and Johnson, K. W. (2013). *Introduction to physics.* Wiley, Hoboken, N.J, 9th ed. edition.

Dickson, R. R., Osborn, T. J., Hurrell, J. W., Meinke, J., Blindheim, J., Adlandsvik, B., Vinje, T., Alekseev, G., and Maslowski, W. (2000). The Arctic Ocean response to the North Atlantic Oscillation. *Journal of Climate*, 13(15):2671–2696.

Dmitrenko, I. A., Polyakov, I. V., Kirillov, S. A., Timokhov, L. A., Frolov, I. E., Sokolov, V. T., Simmons, H. L., Ivanov, V. V., and Walsh, D. (2008). Toward a warmer Arctic Ocean: Spreading of the early 21st century Atlantic water warm anomaly along the Eurasian basin margins. *Journal of Geophysical Research: Oceans*, 113(5):C05023.

Fahrbach, E., Meincke, J., Österhus, S., Rohardt, G., Schauer, U., Tverberg, V., Verduin, J., and Woodgate, R. a. (2001). Direct measurements of heat and mass transports through the Fram Strait. *Polar Research*, 20(2):217–224.

Farrelly, B., Gammelsrød, T., Golmen, L. G., and Sjøberg, B. (1985). Hydrographic conditions in the Fram Strait, summer 1982. *Polar Research*, 3(2):227–238.

Fer, I. (2009). Weak vertical diffusion allows maintenance of cold halocline in the central Arctic. *Atmospheric and Ocean Science Letters*, 2(3):148–152.

Fer, I. (2014). Near-Inertial Mixing in the Central Arctic Ocean. *Journal of Physical Oceanography*, 44(8):2031–2049.

Fer, I. (2015). Cruise HM 2015617 with R.V. Håkon Mosby. Cruise report, Geophysical Institute, University of Bergen.

Fer, I., Peterson, A. K., and Ullgren, J. E. (2014). Microstructure measurements from an underwater glider in the turbulent Faroe Bank Channel overflow. *Journal of Atmospheric and Oceanic Technology*, 31(5):1128–1150.

Firing, E., Ranada, J., and Caldwell, P. (1995). Processing Adcp Data With the Codas Software System Version 3.1. page 226.

Haidvogel, D. B. and Keffer, T. (1984). Tracer dispersal by mid-ocean mesoscale eddies. Part I. Ensemble statistics. *Dynamics of Atmospheres and Oceans*, 8(1):1–40.

Hattermann, T., Isachsen, P. E., Von Appen, W. J., Albretsen, J., and Sundfjord, A. (2016). Eddy-driven recirculation of Atlantic Water in Fram Strait. *Geophysical Research Letters*, 43(7):3406–3414.

Helland-Hansen, B. and Nansen, F. (1912). The Sea West of Spitsbergen, The Oceanographic Observations of the Isachsen Spitsbergen Expedition in 1910. *Vetenskapsselskpaets Skrifter. I. Mat.-Maturv. Klasse*, 1912:12(12):89.

Hilmer, M. and Jung, T. (2000). Evidence for a recent change in the link between the North Atlantic Oscillation and Arctic sea ice export - e Kwok and. *Atlantic*, 27(7):989–992.

Jakobsson, M., Mayer, L., Coakley, B., Dowdeswell, J. A., Forbes, S., Fridman, B., Hodnesdal, H., Noormets, R., Pedersen, R., Rebesco, M., Schenke, H. W., Zarayskaya, Y., Accettella, D., Armstrong, A., Anderson, R. M., Beinhoff, P., Camerlenghi, A., Church, I., Edwards, M., Gerdner, J. V., Hall, J. K., Hell, B., Hestvik, O., Kristoffersen, Y., Marcussen, C., Mohammad, R., Mosher, D., Ngheim, S. V., Pedrosa, M. T., Travaglini, P. G., and Weatherall, P. (2012). The International Bathymetric Chart of the Arctic Ocean (IBCAO) Version 3.0. *Geophysical Research Letters*, 39(12):1–6.

Krishfield, R. A. and Perovich, D. K. (2005). Spatial and temporal variability of oceanic heat flux to the Arctic ice pack. *Journal of Geophysical Research C: Oceans*, 110(7):1–20.

Lenn, Y. D., Wiles, P. J., Torres-Valdes, S., Abrahamsen, E. P., Rippeth, T. P., Simpson, J. H., Bacon, S., Laxon, S. W., Polyakov, I., Ivanov, V., and Kirillov, S. (2009). Vertical mixing at intermediate depths in the Arctic boundary current. *Geophysical Research Letters*, 36(5):L05601.

McDougall, T. J. and Barker, P. M. (2011). *Getting started with TEOS-10 and the Gibbs Seawater (GSW) Oceanographic Toolbox*. SCOR/IAPSO WG127.

Meyer, A., Sundfjord, A., Fer, I., Provost, C., Robineau, V., Koenig, Z., Onarheim, I. H., Lars, H., Duarte, P., Dodd, P. A., and Graham, R. M. (2016). Winter to summer hydrographic and current observations in the Arctic Ocean north of Svalbard. *Journal of Geophysical Research: Oceans*, pages 1–49.

Nasmyth, P. W. (1970). *Ocean turbulence*. PhD thesis, University of British Columbia.

NOAA (2017). Monthly Isopycnal & Mixed-layer Ocean Climatology (MIMOC) — National Oceanic and Atmospheric Administration (NOAA). `https://www.pmel.noaa.gov/mimoc/`. [Online; accessed 15-March-2017].

Onarheim, I. H., Smedsrud, L. H., Ingvaldsen, R. B., and Nilsen, F. (2014). Loss of sea ice during winter north of Svalbard. *Tellus, Series A: Dynamic Meteorology and Oceanography*, 66(1):1–9.

Padman, L. (2004). A barotropic inverse tidal model for the Arctic Ocean. *Geophysical Research Letters*, 31(2):2–5.

Padman, L. and Dillon, T. M. (1991). Turbulent mixing near the Yermak Plateau during the Coordinated Eastern Arctic Experiment. *Journal of Geophysical Research: Oceans*, 96(C3):4769–4782.

Peralta-Ferriz, C. and Woodgate, R. A. (2015). Seasonal and interannual variability of pan-Arctic surface mixed layer properties from 1979 to 2012 from hydrographic data, and the dominance of stratification for multiyear mixed layer depth shoaling. *Progress in Oceanography*, 134:19–53.

Perkin, R. G. and Lewis, E. L. (1984). Mixing in the West Spitsbergen Current. *Journal of Physical Oceanography*, 14(8):1315–1325.

Pnyushkov, A. V., Polyakov, I. V., Ivanov, V. V., Aksenov, Y., Coward, A. C., Janout, M., and Rabe, B. (2015). Structure and variability of the boundary current in the Eurasian Basin of the Arctic Ocean. *Deep-Sea Research Part I: Oceanographic Research Papers*, 101:80–97.

Rainville, L., Lee, C., and Woodgate, R. (2011). Impact of wind-driven mixing in the Arctic Ocean. *Oceanography*, 24(3):136–145.

Rudels, B., Björk, G., Nilsson, J., Winsor, P., Lake, I., and Nohr, C. (2005). The interaction between waters from the Arctic Ocean and the Nordic Seas north of Fram Strait and along the East Greenland Current: results from the Arctic Ocean-02 Oden expedition. *Journal of Marine Systems*, 55(1–2):1–30.

Saloranta, T. M. and Haugan, P. M. (2001). Interannual variability in the hydrography of Atlantic water northwest of Svalbard. *Journal of Geophysical Research*, 106(C7):13931.

Saloranta, T. M. and Haugan, P. M. (2004). Northward cooling and freshening of the warm core of the West Spitsbergen Current. *Polar Research*, 23(1):79–88.

Schauer, U. and Beszczynska-Möller, A. (2009). Problems with estimation and interpretation of oceanic heat transport - Conceptual remarks for the case of Fram Strait in the Arctic Ocean. *Ocean Science*, 5(4):487–494.

Schauer, U., Fahrbach, E., Osterhus, S., and Rohardt, G. (2004). Arctic warming through the Fram Strait: Oceanic heat transport from 3 years of measurements. *Journal of Geophysical Research: Oceans*, 109(6):C06026.

Schmidtko, S., Johnson, G. C., and Lyman, J. M. (2013). MIMOC: A global monthly isopycnal upper-ocean climatology with mixed layers. *Journal of Geophysical Research: Oceans*, 118(4):1658–1672.

Serreze, M. C., Barrett, A. P., Slater, A. G., Woodgate, R. A., Aagaard, K., Lammers, R. B., Steele, M., Moritz, R., Meredith, M., and Lee, C. M. (2006). The large-scale freshwater cycle of the Arctic. *Journal of Geophysical Research: Oceans*, 111(11):C11010.

Sirevaag, A. and Fer, I. (2009). Early Spring Oceanic Heat Fluxes and Mixing Observed from Drift Stations North of Svalbard. *Journal of Physical Oceanography*, 39(12):3049–3069.

Swift, J. H. and Aagaard, K. (1981). Seasonal transitions and water mass formation in the Iceland and Greenland seas. *Deep Sea Research Part A, Oceanographic Research Papers*, 28(10):1107–1129.

Thomas, D. N. and Dieckmann S., G. (2009). *Sea Ice.* Wiley-Blackwell, Chichester, UK.

Thomson, R. E. and Emery, W. J. (2014). *Data analysis methods in physical oceanography.* Elsevier Science, 3rd edition.

Thorpe, S. A. (2007). *An introduction to ocean turbulence.* Cambridge University Press, Cambridge.

Thurnherr, A. M. (2010). A Practical Assessment of the Errors Associated with Full-Depth LADCP Profiles Obtained Using Teledyne RDI Workhorse Acoustic Doppler Current Profilers. *Journal of Atmospheric and Oceanic Technology*, 27(7):1215–1227.

Våge, K., Pickart, R. S., Pavlov, V., Lin, P., Torres, D. J., Ingvaldsen, R., Sundfjord, A., and Proshutinsky, A. (2016). The Atlantic Water boundary current in the Nansen Basin: Transport and mechanisms of lateral exchange. *Journal of Geophysical Research: Oceans*, 121(9):6946–6960.

Visbeck, M. (2002). Deep velocity profiling using lowered acoustic Doppler current profilers: Bottom track and inverse solutions. *Journal of Atmospheric and Oceanic Technology*, 19(5):794–807.

von Appen, W.-J. and Pickart, R. S. (2012). Two Configurations of the Western Arctic Shelfbreak Current in Summer. *Journal of Physical Oceanography*, 42(3):329–351.

von Appen, W.-J., Schauer, U., Hattermann, T., and Beszczynska-Möller, A. (2016). Seasonal Cycle of Mesoscale Instability of the West Spitsbergen Current. *Journal of Physical Oceanography*, 46(4):1231–1254.

Wolk, F., Yamazaki, H., Seuront, L., and Lueck, R. G. (2002). A new free-fall profiler for measuring biophysical microstructure. *Journal of Atmospheric and Oceanic Technology*, 19(5):780–793.

Woodgate, R. (2013). Arctic Ocean Circulation: Going Around At the Top Of the World. *The Nature Education Knowledge Project*, 4.